INTERPRETATION OF COMPLEX RESISTIVITY OF ROCKS USING GEMTIP ANALYSIS

by

Haiyan Fu

A thesis submitted to the faculty of
The University of Utah
in partial fulfillment of the requirements for the degree of

Master of Science

in

Geophysics

Department of Geology and Geophysics

The University of Utah

August 2013

The University of Utah Graduate School

STATEMENT OF THESIS APPROVAL

The thesis of **Haiyan Fu**

has been approved by the following supervisory committee members:

Michael S. Zhdanov	, Chair	**4/29/2013** Date Approved
Vladimir Burtman	, Member	**4/24/2013** Date Approved
Erich U. Petersen	, Member	**4/24/2013** Date Approved

and by **D. Kip Solomon** , Chair of

the Department of **Geology and Geophysics**

and by Donna M. White, Interim Dean of The Graduate School.

ABSTRACT

The induced polarization (IP) effect, in general, is related to the complex resistivity of rocks. Modeling IP phenomena is important for developing effective methods for remote sensing of subsurface geology. The Generalized Effective Medium Theory of Induced Polarization (GEMTIP) has been derived based on the effective medium approach to the characterization of heterogeneous, multiphase, polarized medium typical in rock formations. It describes the relationships between petrophysical and structural properties of rock and the parameters of the corresponding resistivity relaxation model (Zhdanov, 2008). The parameters of the GEMTIP model are determined by the intrinsic petrophysical and geometrical characteristics of the medium: the mineralization, the matrix composition, porosity, anisotropy, and polarizability of the formations. In this paper, two igneous rock samples and three shale samples were tested by the randomly oriented ellipsoidal GEMTIP model, both two-phases and three-phases models were used in the study. Inversion routines were developed and tested using synthetic data to recover the three variables: volume fraction (f), relaxation parameters (C), and time constant (τ). Both Regularized Conjugate Gradient (RCG) method and extensive search method were implemented in the study.

Complex resistivity were calculated from recorded EM data from 0.005 Hz to 10000 Hz at 33 different frequencies, detailed geologic analysis using Quantitative Evaluation of Materials using Scanning Electron Microscope (QEMSCAN) and X-ray is conducted to determine GEMTIP model parameters and help better understand the inversion results. The application of shale samples shows that the shale samples are characterized by a significant IP response, and the GEMTIP model can be applied to hydrocarbon bearing shale rocks. The results of our study show that the ellipsoidal GEMTIP model can successfully interpret the IP effect of the mineral rocks and shale samples. By comparing the two-phases with three-phases inversion results, the mineral rock samples study shows that the three-phases model can separate the different mineral sizes and different mineral types from the same sample, the shale samples show the three-phases GEMTIP model can separate the membrane polarization caused by the internal structure of the shale samples from electrode polarization caused by disseminated pyrite. The GEMTIP parameter time constant increases with increases of the grain size. Successful GEMTIP model of the rock samples provided insight into controlling factors of the IP effect.

CONTENTS

ABSTRACT .... **iii**

LIST OF TABLES .... **vii**

ACKNOWLEDGMENTS .... **viii**

CHAPTERS

1. EFFECTIVE MEDIUM THEORY OF COMPLEX RESISTIVITY ROCKS **1**

1.1 Introduction 1
1.2 The induced polarization effect 2
1.3 Methods of measurement of IP effect 6
1.4 GEMTIP modeling 14

2. FORWARD MODELING AND INVERSION OF SYNTHETIC DATA **22**

2.1 Forward modeling: GEMTIP model 22
2.2 Regularized conjugate gradient method 30
2.3 Inversion: synthetic data 32

3. DATA ACQUISITION METHODOLOGY **39**

3.1 Description of the samples 39
3.2 Sample preparation for complex resistivity analysis 46
3.3 QEMSCAN measurement 48
3.4 Complex resistivity measurement 56

4. INVERSION RESULT **61**

4.1 Igneous rock samples 61
4.2 Shale samples 68
4.3 Discussion 77

5. CONCLUSIONS **79**

APPENDICES

A. INVERSION RESULT **81**

B. LIST OF ELECTRONIC DATA 83

REFERENCES 84

LIST OF TABLES

Table **Page**

1.1 Descriptive guide for GEMTIP parameters 18

2.1 GEMTIP parameters used when varying ellipticity (e) 23

2.2 GEMTIP parameters used when varying volume fraction (f) 23

2.3 GEMTIP parameters used when varying relaxation parameters (C) 23

2.4 GEMTIP parameters used when varying time constant (τ). 24

2.5 GEMTIP parameters used when varying resistivity (ρ_0)............ 24

2.6 GEMTIP two-phases synthetic data inversion result............ 33

2.7 Three-phases synthetic data inversion result 36

3.1 K01 mineralogical summary 42

3.2 Sample mineralogy by X-ray diffraction (weight%) 45

3.3 Sample mineralogy by QEMSCAN............ 51

4.1 Inversion parameters for sample K01 using the ellipsodial GEMTIP model............ 64

4.2 Inversion parameters for sample #13 using the ellipsodial GEMTIP model............ 67

4.3 Inversion parameters for sample #8 using the ellipsodial GEMTIP model............ 70

4.4 Inversion parameters for sample #33 using the ellipsodial GEMTIP model............ 73

4.5 Inversion parameters for sample #45 using the ellipsodial GEMTIP model............ 76

4.6 GEMTIP parameters value of shale samples............ 78

A.1 Two-phases inversion result............81

A.2 Three-phases inversion result............82

ACKNOWLEDGMENTS

I would like to thank the Consortium for Electromagnetic Modeling and Inversion (CEMI) at the University of Utah for the financial and technical support.

I give many thanks to my adviser and committee chair, Dr. Michael Zhdanov, for his expert guidance and direction. I am also grateful for the inspiring classes that he taught on electromagnetic and inversion theory.

Thanks to Dr. Alex Gribenko and Dr. Xiaojun Liu for providing the original Matlab code.

Special thanks must go to Vladimir Burtman for helping me understand rock physics, to Dr. Erich Petersen for providing the time on the QEMSCAN equipment.

Thanks to all those who helped in the development of this thesis project.

CHAPTER 1

EFFECTIVE MEDIUM THEORY OF COMPLEX RESISTIVITY OF ROCKS

1.1 Introduction

The electromagnetic (EM) data observed in geophysical experiments generally reflect two phenomena: (1) electromagnetic induction (EMI) in the earth and (2) the induced polarization (IP) effect related to the relaxation of polarized charges in rock formations. The IP effect, in general, is related to the complex resistivity of rocks. It is an important tool for mineral exploration and has been utilized for over 50 years. IP surveys can be more sensitive to mineralization, pore fluids, and more compared to direct current (DC) resistivity surveys. The phenomenon was first noticed by Schlumberger in the early 20th century. James Wait describes his first exposure to the IP effect when Yanzhong Luo and Dr. Guiqing Zhang, after carrying out careful sample measurements on the effective resistivity of a wetted rock sample, showed him that there was a "strange" frequency dependence. Wait then coined the phrase "complex resistivity" because it had both amplitude and phase (Luo et al., 1998). Over the years models have been proposed to describe the IP effect, the Cole-Cole model first adopted by Pelton (Pelton et al., 1978) is a well-accepted empirical model. Most models describing the IP are empirical, the newly developed Generalized Effective Medium Theory of IP by Zhdanov (2008) were tested in the following chapters. The generalized effective medium theory for induced polarization (GEMTIP) enables one to model and invert the complex resistivity (CR) spectra for rock and fluid parameters such as matrix resistivity, grain size, grain resistivity, fraction volumes, porosity, fluid saturations, and polarizability. Moreover, GEMTIP can explain anisotropic resistivity in terms of grain orientation. In this paper, the GEMTIP model is used to invert laboratory-based complex resistivity measurements for the aforementioned rock properties. We have applied the GEMTIP model to analyze the IP phenomena in mineralized rocks and hydrocarbon bearing rocks. From laboratory measurements of rock samples, we show how the mineral properties recovered from GEMTIP analyses of CR spectra can be correlated with optical microscopy, Quantitative Evaluation of Minerals by Scanning Electron Microscopy (QEMSCAN) and x-ray tomographic mineralogical analyses. This enables us to potentially better understand the IP mechanisms of different types of rock samples.

1.2 The induced polarization effect

Induced polarization (IP) is a geophysical phenomenon that is manifested by the slow decay of voltage in the ground after the cessation of an excitation current pulse in time domain method or low frequency variation of the resistivity of the earth in frequency domain method (Sumner, 1976). When using a standard four-electrode resistivity spread in a DC mode, if the current is abruptly switched off, the voltage between the potential electrodes does not drop to zero immediately. After a large initial decrease the voltage suffers a gradual decay and can take many seconds to reach a zero value. A similar phenomenon is observed as the current is switched on. After an initial sudden voltage increase, the voltage increases gradually over a discrete time interval to a steady-state value. The ground thus acts as a capacitor and stores electrical charge, that is, becomes electrically polarized.

If instead of using a DC source for the measurement of resistivity, a variable low-frequency alternating current (AC) source is used, it is found that the measured apparent resistivity of the subsurface decreases as the frequency is increased. This is because the capacitance of the ground inhibits the passage of direct currents but transmits altering currents with increasing efficiency as the frequency rises. The capacitive property of the ground causes both the transient decay of a residual voltage and the variation of apparent resistivity as a function of frequency. The two effects are representations of the same phenomenon in the time and frequency domain, and are linked by Fourier transformation (Kearey, 2002). These two manifestations of the capacitance property of the ground provide two different survey methods for the investigation of the effect.

The exact cause of the IP effect is complicated. It can be basically defined as current flow accompanied by complex electrochemical reactions and charge build up at interfaces, grain boundaries, vein walls, and other boundaries. The polarizable behavior (IP effect) of a disseminated mineralization and a mineralized vein is shown in Figure 1.1. Over the years laboratory experiments indicate that electrical energy is stored in rocks by one of two main mechanisms of electrochemical processes, the first being electrode (or grain) polarization, and the second being membrane (or electrolytic) polarization.

When metallic minerals are present in a rock, an alternative, electronic path is available for current flow. Figure 1.1 (a) shows a rock in which a metallic mineral grain

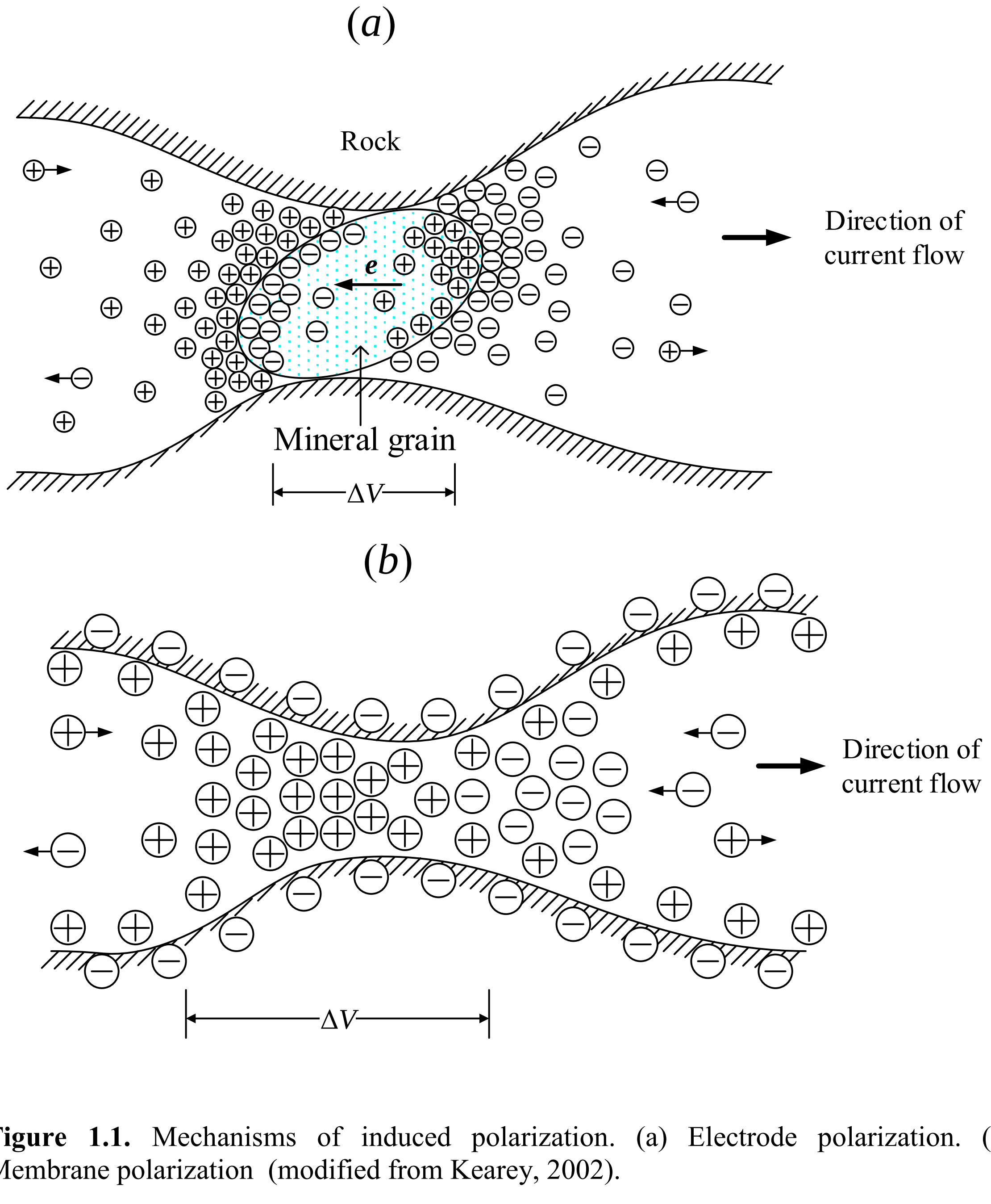

Figure 1.1. Mechanisms of induced polarization. (a) Electrode polarization. (b) Membrane polarization (modified from Kearey, 2002).

blocks a pore space. When a voltage is applied to either side of the pore space, positive and negative charges are imposed on opposite sides of the grain. Negative and positive ions then accumulate on either side of the grain, which is attempting either to release electrons to the grain or to accept electrons conducted through the grain. The rate at which the electrons are conducted is slower than the rate of electron exchange with the ions. Consequently, ions accumulate on either side of the grain and cause a buildup of charge, thus impeding current flow. When the voltage is removed the ions slowly diffuse back to their original locations and cause a time delayed decaying voltage. This is analogous to the capacitor effect. This effect is known as electrode polarization or overvoltage. All minerals which are good conductors (e.g., metallic sulphides, graphite and oxides) contribute to this effect. The magnitude of the electrode polarization effect depends upon both the magnitude of the impressed voltage and the mineral concentration. Foremost among the ore mineral having an electronic mode of conduction and therefore exhibiting strong IP are pyrite, pyrrhotite, chalcopyrite, graphite, galena, bornite, and magnetite. It is most pronounced when the mineral is disseminated throughout the host rock as the surface area available for ionic-electronic interchange is then at a maximum. The effect decreases with increasing porosity as more alternative paths become available for the more efficient ionic conduction (Kearey, 2002).

The passage of current through a rock as a result of an externally imposed voltage is accomplished mainly by electrolytic flow in the pore fluid. Most of the rock forming minerals have a net negative charge on their outer surfaces, which are in contact with the pore fluid and attract positive ions within the pore fluid onto this surface and build up a positively charged layer up to about 100 micro thick, while negative charges are repelled

(Figure 1.1 b). If the pore channel diameter reduces to less than this distance, the constriction will block the flow of ions when a voltage is applied. Negative ions will leave the constricted zone and positive ions will increase their concentration, so producing a potential difference across the blockage. When the applied voltage is switched off, the imbalance in ionic concentration is returned to normal by diffusion, which produces the measured IP response. This effect is known as membrane polarization. It is most pronounced in the presence of clay minerals (sedimentary rocks) where the pores are particularly small. This effect also decreases with the increasing salinity of the pore fluid (Kearey, 2002). This type of polarization explains the IP effects that are observed when no metallic type grain is present.

1.3 Methods of measurement of IP effect

In theory, induced polarization is a dimensionless quantity, whereas in practice it is measured as a change in voltage with time or frequency. The time and frequency IP methods are fundamentally similar; however, they differ in a way of considering and measuring electrical waveforms. In the former, a direct current is applied into the ground, and what is recorded is the decay of voltage between two potential electrodes after the cut off of the current (time domain method). In the latter, the variation of apparent resistivity of the ground with two or more low alternating current (AC) frequency of the applied current is determined (frequency domain method). In another type of frequency method, which is called Complex Resistivity (CR) method, a current at frequency range (0.001 Hz to 10 kHz) is injected into the ground and the amplitude of voltage as well as its phase with respect to the current is measured. That is a phase-angle IP measurement. It is important to note that many CR implementations are measuring the real and quadrature component of the response. Of course it is very easy to transform these two parameters into amplitude and phase.

1.3.1 Time domain method

When using a standard four-electrode resistivity array in direct current (DC) mode, the voltage between the potential electrodes does not drop to zero immediately if the current is abruptly switched off. After a large initial decrease the voltage suffers a gradual decay as stated previously and can take many seconds to reach a zero value (Figure 1.2). A similar phenomenon is observed as the current is switched on. When the current is injected (turn on signal in the source) into the ground, the potential rises up immediately, but it takes some time to reach the maximum (steady state voltage value). The ground thus acts as a giant capacitor and stores electrical charge, or rather, becomes electrically polarized. This observation is known as the overvoltage effect in the time domain. The length of time required for the overvoltage ($\mathrm{V_s}$) to drop is recorded and the time domain chargeability is defined as the ratio of the potential at some time after turn off of the current to the steady state value of the potential.

$$\mathrm{M} = \frac{\mathrm{V_s}}{\mathrm{V_p}}\ (\mathrm{mV/V}) \tag{1.1}$$

where $\mathrm{V_p}$ is the steady state value of voltage, and $\mathrm{V_s}$ is the consequent measured overvoltage. Instrumentally, it is extremely difficult to measure $\mathrm{V_s}$ at the moment the current is switched off due to electromagnetic effects which produce a transient disturbance on switching, so it is measured at specific times after cut off. Measurements are then made of the decay of $\mathrm{V_s}$ over a very short time period after discrete intervals of t-

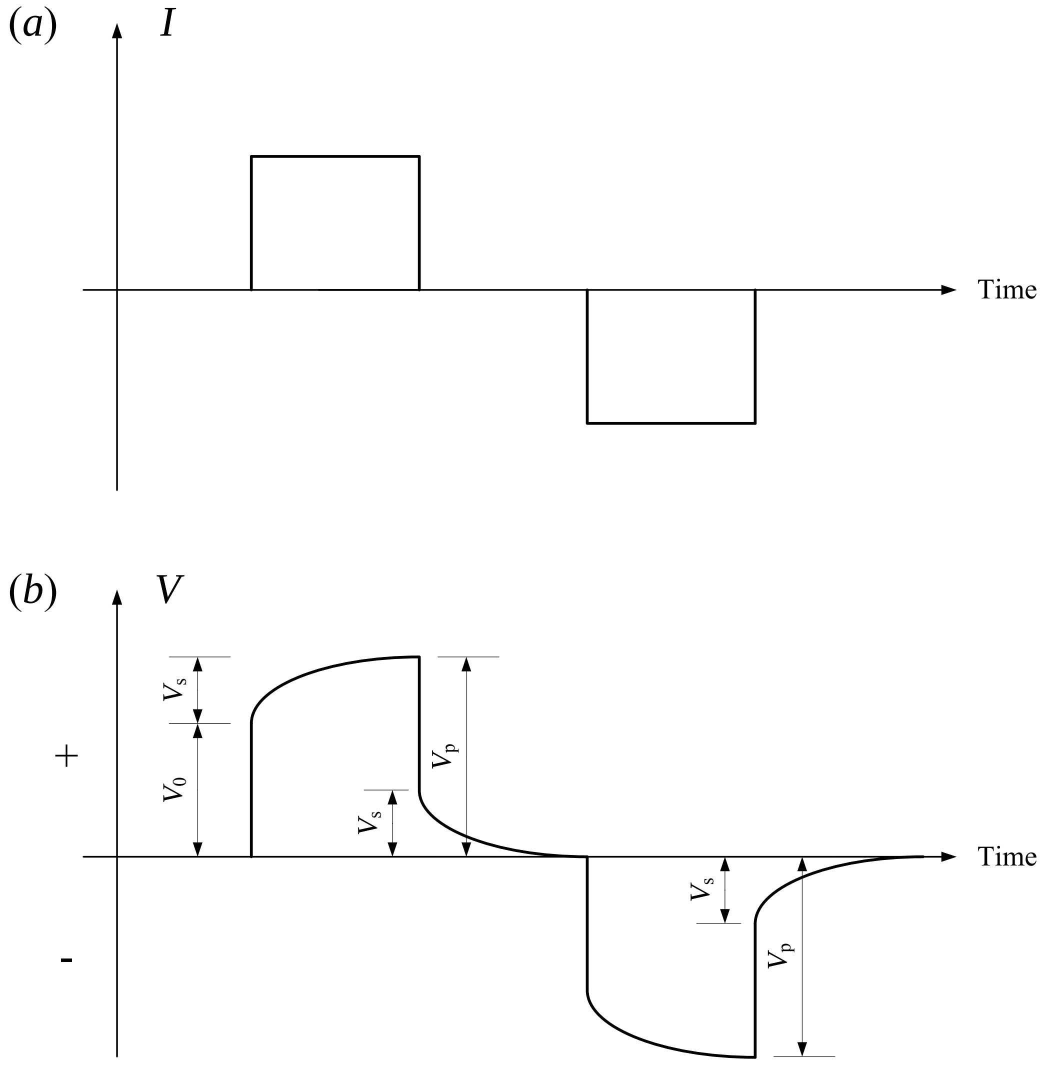

Figure 1.2. Representation of IP effect in time domain (modified from Zhdanov, 2008). (a) Transmitted current waveform versus time. (b) Recorded voltage waveform versus time.

ime. The measured parameter in the time domain is the area under the decay curve of voltage $V_{s(t)}$ corresponding to the time interval (t1, t2). The integration of these values with respect to time gives the area under the curve (Figure 1.3), which is an alternative way of defining the curve. When the integral is divided by V_p, the resultant value is called the chargeability (m) . It is expressed as:

$$m = \frac{1}{V_p} \int_{t_1}^{t_2} V_{s(t)} dt = \frac{A}{V_p} \tag{1.2}$$

where V_s is the off-time measured MN voltage at time t, and V_p the observed voltage with an applied current. Where AB is the current injection dipole and MN is the voltage measuring dipole. Note, however, the major advantage of integration and normalizing by V_p is that the noise from cross coupling of cables and from background potentials is reduced. Care has to be exercised in selecting appropriate time intervals to maximize signal to noise ratios without reducing the method's diagnostic sensitivity.

1.3.2 Frequency domain method

IP effects can be observed in the frequency domain. Instead of using a DC source for the measurement of resistivity, a variable low frequency alternating current source is used; it is found that the measured apparent resistivity (equation 1.3) of the subsurface decreases as the frequency increases (Sumner, 1976). In equation 1.3, K describes a geometric factor of the array configuration, U is the potential difference and I is the current strength. This occurs because the capacitance of the ground inhibits the passage of direct currents but transmits alternating currents with increasing efficiency as the frequency rises.

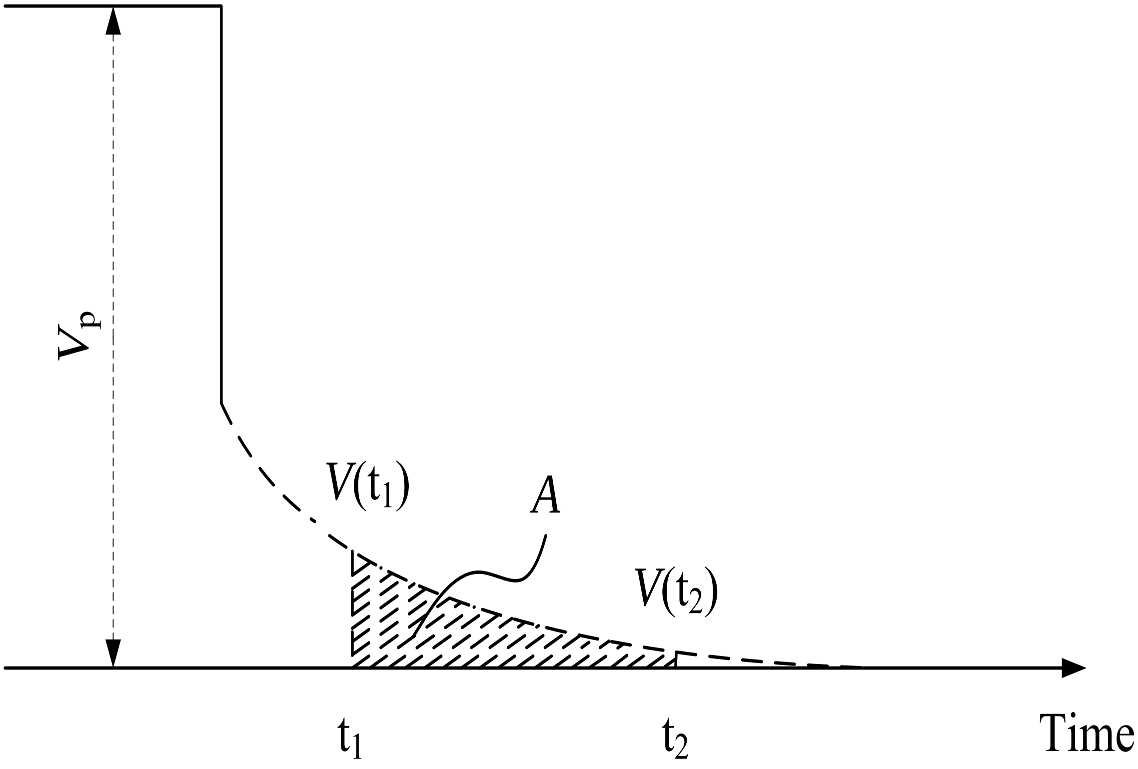

Figure 1.3. The integrated decay voltage curve used as a measurement of chargeability (modified after Reynolds, 1997).

$$\rho_{app} = K\frac{U}{I} \tag{1.3}$$

Usually it is common to compare the impedance at some alternating frequency with that of some very low frequency which is often referred to as the DC impedance. The effect is then evaluated as a certain percentage increase in the conductance at the frequency (Zonge et al., 1972). The applied current is generally sampled at two frequencies, each at a decade apart and less than 10Hz (Zonge et al., 1972). The measurements are made at low frequencies because we can then assume that the term dB/dt at the Maxwell's equations can be neglected. The waveform that is recorded at the receiver is a combination of both the applied current and a phase difference. This phase angle seen in the frequency-domain, shown in Figure 1.4, is the equivalent of the chargeability quantity observed in the time domain measurements (Sumner, 1976).

This difference in the phase is caused by the differences in the subsurface geology. The following formula characterizes the phase difference:

$$\mathrm{FE} = \frac{\mathrm{V}_2 - \mathrm{V}_1}{\mathrm{V}_1} \tag{1.4}$$

where V_2 is the observed voltage, V_1 is the implied voltage, we called the parameter FE, frequency effect.

Another representation of IP effect in the frequency domain is Percent Frequency Effect (PFE), which is defined as the relative difference between the apparent resistivity with a higher frequency from that with a lower frequency, normalized by the apparent resistivity with the high frequency in percent. It can be expressed as:

$$\mathrm{PFE} = \frac{\rho_{f1} - \rho_{f2}}{\rho_{f1}} * 100 \tag{1.5}$$

Because time and frequency domain data are related to each other, when the phenomenon is linear, through the Fourier transform, we can expect to derive frequency information from the transient measurements or vice versa. There is not an exact one to one correspondence between a point in the frequency domain, and a point in the time domain, but there is often an approximate one. For example, the percentage frequency effect (PFE) and the mv/volt parameters are found to be closely related (Madden and Marshall, 1958).

Note that the conventional IP method in the frequency domain is very similar to the DC resistivity survey and IP data acquisition systems and interpretation techniques are very similar to those of the DC resistivity methods (VES).

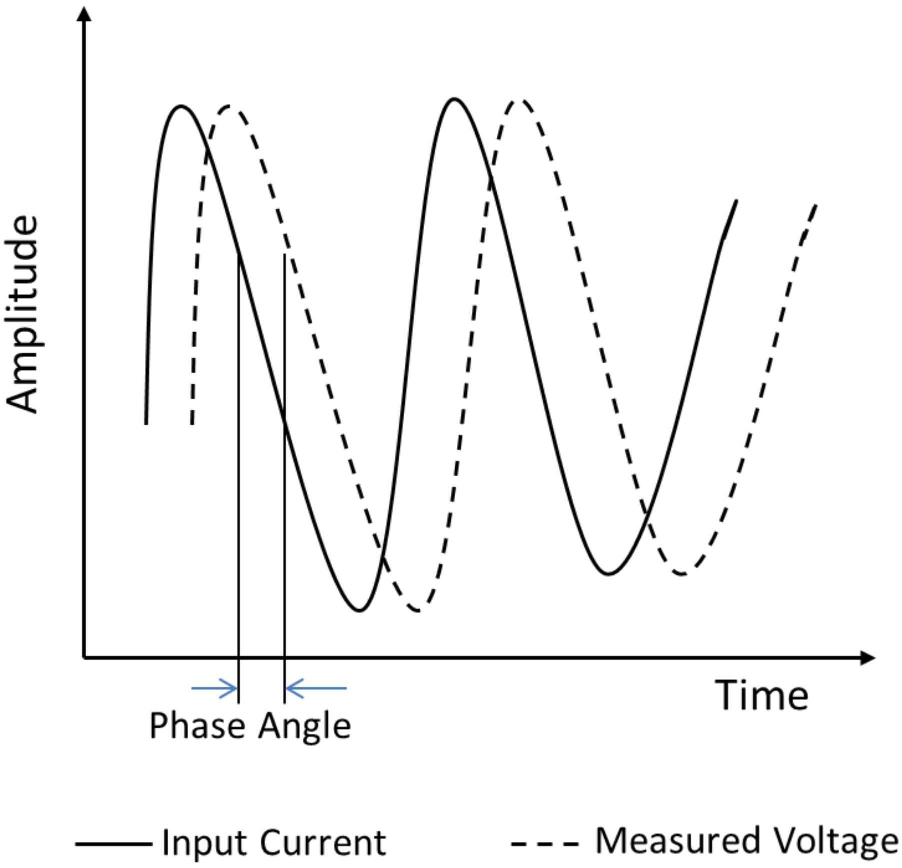

Figure 1.4. Frequency domain IP measurements. The waveform of an applied alternating current and the waveform of the corresponding measured voltage at the receiver are observed and the phase angle is measured (modified after Sumner 1976).

1.3.3 Complex resistivity (spectral IP) method

This involves taking amplitude and phase measurements, which in IP are defined as the difference in phase angle between the received polarization voltage signal and the stimulating current signal by Ohm's law, in the case when both are sinusoidal waveforms. If the input current is a square wave, the phase measurement is defined as the phase angle between the fundamental harmonic of the transmitted and received signals. Note that, in the presence of the IP effect the measured potential in the frequency domain is complex; therefore, the apparent resistivity is characterized by a complex number as well:

$$\rho_a(\omega) = \rho_{real}(\omega) + i\rho_{imag}(\omega) \tag{1.6}$$

The phase angle is defined as the angle, whose tangent is the ratio between the imaginary and real components of the received voltage or resistivity and is expressed as:

$$\Phi = \tan^{-1}\frac{V_{imag}}{V_{real}} = \tan^{-1}\frac{\rho_{imag}}{\rho_{real}} \tag{1.7}$$

The in–phase (real) and the out–of–phase (imaginary) components are more easily measured with modern electronic systems than the phase angle alone and the two components provide additional useful information about IP phenomena. The magnitude of the complex apparent resistivity is the same as the DC apparent resistivity. In my project, the voltage amplitude (V_1, V_2) and phase (Φ) are measured over a wide range of frequencies (0.005 to 10 kHz) of applied current.

A reference resistor is used in the process of measurement. The magnitude of the real part of resistivity is determined by equation 1.8:

$$\rho_{real} = R_{ref} * \left(\frac{V_2 - V_1}{V_1}\right) * \frac{S}{L} \tag{1.8}$$

where R_{ref} is reference resistor resistivity, S is cross section area of the measured sample, and L is the length of the measured sample.

According to the above equation, we can get the imaginary part of resistivity.

$$\rho_{imag} = \rho_{real} * \tan(\Phi) \tag{1.9}$$

To sum up, there are three methods of measurement of IP effect that have been discussed. Chargeability being the measured parameter in the time domain measurements as the percentage frequency effect is for the frequency domain measurements. Complex resistivity (CR) is the third measurement method in which the magnitude of the complex resistivity and the phase of polarization voltage are measured over a wide range of frequencies.

1.4 GEMTIP modeling

An important problem of electromagnetic geophysics is to study the frequency dependent complex resistivity of rocks, in which the IP phenomenon is often manifested. As mentioned before, over the last 50 years several conductivity relaxation models have been developed. Such models include the empirical Cole-Cole model (Cole and Cole, 1941; Pelton et al., 1978), electrochemical models developed by Ostrander and Zonge (1978), and the generalized effective-medium theory of induced polarization (GEMTIP). GEMTIP is a new, rigorous, mathematically formulated conductivity model introduced by Zhdanov (2008).

The widely accepted Cole-Cole model uses bulk rock variables and does not address rock composition, while the GEMTIP model uses effective-medium theory to describe the complex resistivity of heterogeneous rocks. The GEMTIP resistivity model incorporates the physical and electrical characteristics of rocks at the grain scale into an analytic expression. These characteristics include grain size, grain shape, mineral conductivity, porosity, anisotropy, polarizability, mineral volume fraction, pore fluids, and more (Zhdanov, 2008).

Following the principles of the GEMTIP approach, we represent a complex heterogeneous rock formation as a composite model formed by a homogeneous host medium of a volume V with a complex conductivity tensor $\hat{\sigma}_0(\mathrm{r})$ (where r is an observation point) filled with grains of arbitrary shape and conductivity. The rock is composed of a set of N different types of grains, the lth grain type having a complex tensor conductivity $\widehat{\sigma}_l(r)$. The grains of the lth type have a volume fraction f_l in the medium and a particular shape and orientation. The polarizability effect is usually associated with surface polarization of the coatings of the grains. This surface polarization can be related to electrochemical charge transfer between the grains and a host medium. The surface polarization is manifested by accumulating electric charges on the surface of the grain. A double layer of charges is created on the grain's surface, which results in the voltage drop at this surface. The polarizability effect is quantitatively represented in the fundamental equations of the GEMTIP model through the volume depolarization tensor, $\widehat{\Gamma}_l$, and a surface polarizability tensor $\widehat{p}$ (Zhdanov, 2008). A general solution of the effective conductivity problem for an arbitrary multiphase composite polarized medium is provided by the following expression:

$$\widehat{\sigma}_e = \widehat{\sigma}_0 + \sum_{l=1}^{N} \left[\hat{I} + \widehat{p}_l\right]^{-1} \left[\hat{I} - \Delta\widehat{\sigma}_l^p \cdot \widehat{\Gamma}_l\right]^{-1} \cdot \left[\hat{I} + \widehat{p}_l\right] \cdot \Delta\widehat{\sigma}_l f_l \tag{1.10}$$

where $\Delta\widehat{\sigma}_l = \widehat{\sigma}_l - \widehat{\sigma}_0$ is anomalous conductivity, and $\Delta\widehat{\sigma}_l^p$ is a "polarized" anomalous conductivity:

$$\Delta\widehat{\sigma}^p(r) = \left[\hat{I} + \widehat{p}(r)\right] \cdot \Delta\widehat{\sigma}(r) \tag{1.11}$$

This formula allows us to find the effective conductivity for inclusions with arbitrary shape and electrical properties. That is why the new composite goelectrical model of the IP effect may be used to construct the effective conductivity for realistic rock formations typical for mineralization zones and/or petroleum reservoirs.

In the case of an isotropic multiphase composite model, with all model parameters described by the scalar functions, equation (1.10) can be simplified. For example, if a composite model is formed by a homogeneous host medium of a volume V with a conductivity σ_0 filled with grains of spherical shape, and we assume that we have a set of N different types of grains, the lth grain type having radius a_l, conductivity σ_l, and surface polarizability k_l, the volume depolarization tensors are constant scalar tensors equal to (Zhdanov, 2008):

$$\hat{\Gamma}_l = \Gamma_l \hat{I} = -\frac{1}{3\sigma_b}\hat{I} \tag{1.12}$$

The surface polarizability tensor $\hat{p}_l$ also becomes scalar tensor and equals to:

$$\hat{p}_l = p_l \hat{I} = 2k_l a_l^{-1}\sigma_b\sigma_l(\Delta\sigma_l)^{-1}\hat{I} \tag{1.13}$$

In the last formula, k_l is the surface polarizability factor, which is a complex function of frequency, described for the lth grain by the following formula:

$$k_l = \frac{a_l}{2}(2\rho_l + \rho_0)(i\omega\tau_l)^{-C_l} \tag{1.14}$$

where τ_l is the time constant; C_l is the relaxation parameter; and $\rho_l = 1/\sigma_l$.

Substituting expressions (1.12), (1.13) and (1.14) into a general equation (1.10), after some algebra, we arrive at the following GEMTIP model of the effective resistivity ρ_e for the multiphase composite medium with spherical grains:

$$\rho_e = \rho_0\left\{1 + \sum_{l=1}^{N}\left[f_l m_l\left[1 - \frac{1}{1+(i\omega\tau_l)^{C_l}}\right]\right]\right\}^{-1} \tag{1.15}$$

where:

$$m_l = 3\frac{\rho_0-\rho_l}{2\rho_l+\rho_0}, \tau = \left[\frac{a_l}{2\alpha_l}(2\rho_l + \rho_0)\right]^{\frac{1}{c_l}} \tag{1.16}$$

In the last expressions, ρ_0 is the matrix resistivity of rock, f_l is volume fraction of each grain type, m_l is chargeability of each grain type, a_l is average size of each grain type, α_l is surface polarizability coefficient, τ_l and C_l are time constant and relaxation parameters for each grain, respectively.

In particular, for a simplified two-phase composite model, we have the complex resistivity expression:

$$\rho_e = \rho_0 \left\{1 + p\left[1 - \frac{1}{1+(i\omega\tau_1)^{c_1}}\right]\right\}^{-1} \tag{1.17}$$

where:

$$p = f_1 m_1,\ m_1 = 3\frac{\rho_0 - \rho_1}{2\rho_1 + \rho_0},\ \tau_1 = \left\{\frac{a_1}{2a_1}(2\rho_1 + \rho_0)\right\}^{1/c_1} \tag{1.18}$$

Note that, if the inclusions are conductive,

$$\rho_1 \ll \rho_0 \tag{1.19}$$

The formula is simplified as follows:

$$m_1 = 3\ ,\ \tau_1 = \left\{\frac{a_l}{2\alpha_l}\rho_0\right\}^{1/c_1} \tag{1.20}$$

However, medium with spherical inclusions is the ideal case for minerals. We consider now a medium formed by completely randomly oriented ellipsoids, the effective conductivity of this medium can be calculated by taking an average over the orientations. As a result, we obtain the complex resistivity of randomly oriented ellipsoidal inclusions expression:

$$\rho_e = \rho_0 \left\{1 + \sum_{l=1}^{N} f_l m_l \frac{1}{3} \sum_{a=x,y,z} \frac{2\rho_1 + \rho_0}{3h_a}\left[1 - \frac{1}{1+(i\omega\tau_l)^{c_l}\frac{2h_a}{\lambda_{la}\overline{a_l}(2\rho_1+\rho_0)}}\right]\right\}^{-1} \tag{1.21}$$

where

$$h_a = \rho_1 + \gamma_{la}(\rho_0 - \rho_1) \tag{1.22}$$

with the model parameters being defined in Table 1.1. The coefficients γ_{la}, λ_{la} are depolarization parameters, they are the structural parameters, defined by geometrical characteristics of the ellipsoidal inclusions (Zhdanov, 2008), and they are functions of ellipticity e_l; and $\overline{a_l}$ is an average value of the equatorial (a_{lx} and a_{ly}) and polar (a_{lz}) radius of the ellipsoidal grains, expressed by $\overline{a_l} = \frac{a_{lx}+a_{ly}+a_{lz}}{3}$. Spherical inclusions case

Table 1.1 Descriptive guide for GEMTIP parameters

Variable	Units	Name	Description
ρ_e	Ωm	effective resistivity	resulting effective
ρ_0	Ωm	matrix resistivity	matrix resistivity of rock
f_l	-	grain vol. fraction	vol. fraction of each grain
m_l	-	grain chargeability	chargeability of each grain
ω	Hz	angular frequency	angular frequency of EM
τ_l	s	time constant	time constant for each grain
C_l	-	relaxation parameters	decay coefficient
ρ_l	Ωm	grain resistivity	resistivity of each grain
a_l	m	grain radius	radius of each grain type
α_l	$\Omega m.\, m/_{sec^{C_l}}$	surface polarizability	charge behavior on grain
γ_l	-	volume depolarization parameter	structural character
λ_l	-	surface depolarization parameter	structural character

in reservoir rock for a GEMTIP model are shown in the left panel of Figure 1.5, while the ellipsoidal inclusions are shown in the right panel. If all the grains are oriented in one specific direction as shown in Figure 1.6, panel 2, the effective conductivity of this medium will become anisotropic. Thus, the effective conductivity may be a tensor in spite of the fact that the background medium and all the grains are electrically isotropic.

When we calculate the forward modeling, we introduce new notations:

$$\frac{2h_a}{\lambda_{la}(2\rho_1+\rho_0)} = \frac{2(\rho_1+\gamma_{la}(\rho_0-\rho_1))}{\lambda_{la}(2\rho_1+\rho_0)} \approx \frac{2\gamma_{la}}{\lambda_{la}} = r_a \tag{1.23}$$

where we assume that the inclusions are conductive, also,

$$\frac{2\rho_1+\rho_0}{3h_a} = \frac{2\rho_1+\rho_0}{3(\rho_1+\gamma_{la}(\rho_0-\rho_1))} \approx \frac{1}{3\gamma_{la}} \tag{1.24}$$

Finally we have:

$$\rho_e = \rho_0\left\{1 + p\frac{1}{3}\sum_{a=x,y,z}\frac{1}{3\gamma_{la}}\left[1-\frac{1}{1+(i\omega\tau_l)^{C_l}\frac{r_a}{a_l}}\right]\right\}^{-1} \tag{1.25}$$

where

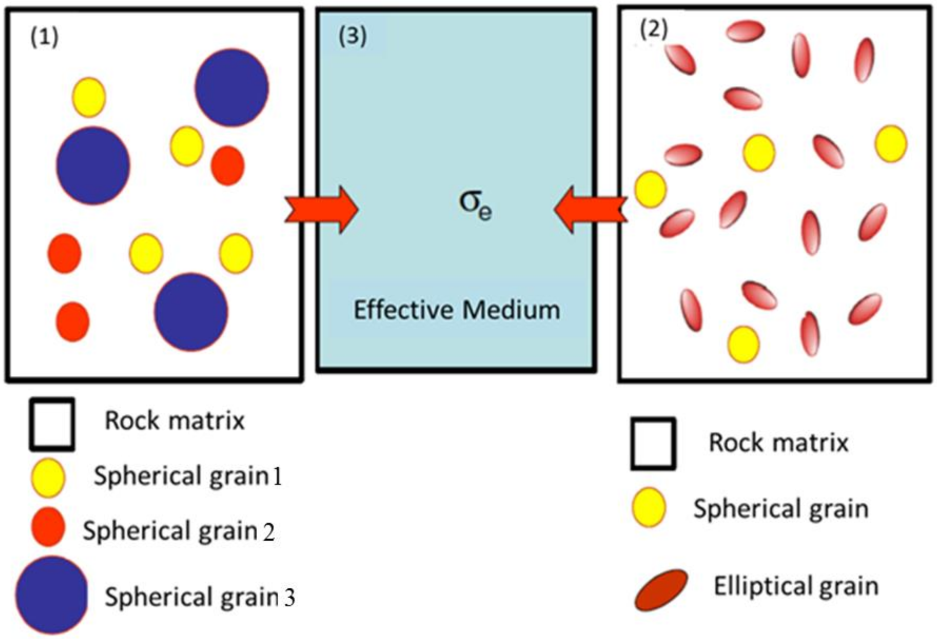

Figure 1.5. An effective medium model of a reservoir rock (shown in the central panel 3) by the GEMTIP model with spherical inclusions (left panel 1) and by the GEMTIP model with ellipsoidal inclusions (right panel 2).

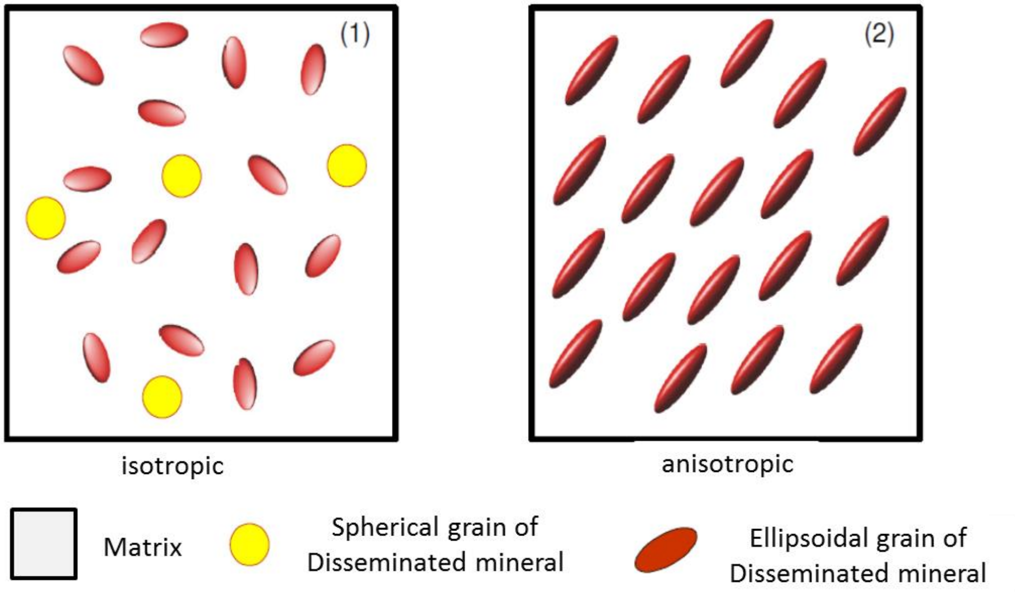

Figure 1.6. Examples of multiphase model of rocks composed of a set of different types of randomly oriented grains (left panel 1) and composed of a set of ellipsoidal grains oriented in one direction (right panel 2).

$$r_a = \frac{2\gamma_{la}}{\lambda_{la}} \tag{1.26}$$

In the following chapter, we use equation (1.25) to do the forward modeling and invert the observed complex resistivity curve. Note that, for spherical inclusions we have:

$$\gamma_{la} = 1/3;\ \lambda_{la} = 2/3a_1;\ \bar{a}_l = a_1;\ r_a = a_1; a = x, y, z\ ; \tag{1.27}$$

equation (1.25) for elliptical grains reduces to equation (1.17) for spherical grains. The test model curve is shown in Figure 1.7.

In the case of spherical grains, the surface polarizability coefficients can be selected in the following form (Zhdanov, 2008):

$$a_l = \frac{a_l}{2}(2\rho_1 + \rho_0)\tau_l{}^{-C_l} \tag{1.28}$$

By analogy, in the case of ellipsoidal grains, we define the empirical surface polarization coefficient a_l as follows:

$$a_l = \frac{\bar{a}_l}{2}(2\rho_1 + \rho_0)/\tau_l{}^{-C_l} \tag{1.29}$$

where $\bar{a}_l$ is an average value of the equatorial and polar radius of the ellipsoidal grain. Understanding induced polarization phenomena is important for developing the methods of subsurface geophysical exploration. With growing interest in this area of explorative geophysics, considerable research has been invested in the understanding of IP phenomena. Only recently has a breakthrough in the application of IP method developed. This breakthrough was introduced initially by Zhdanov (2008) who developed the generalized effective-medium theory of induced polarization incorporating many geoelectric parameters. This new model is tested and applied in the following chapters.

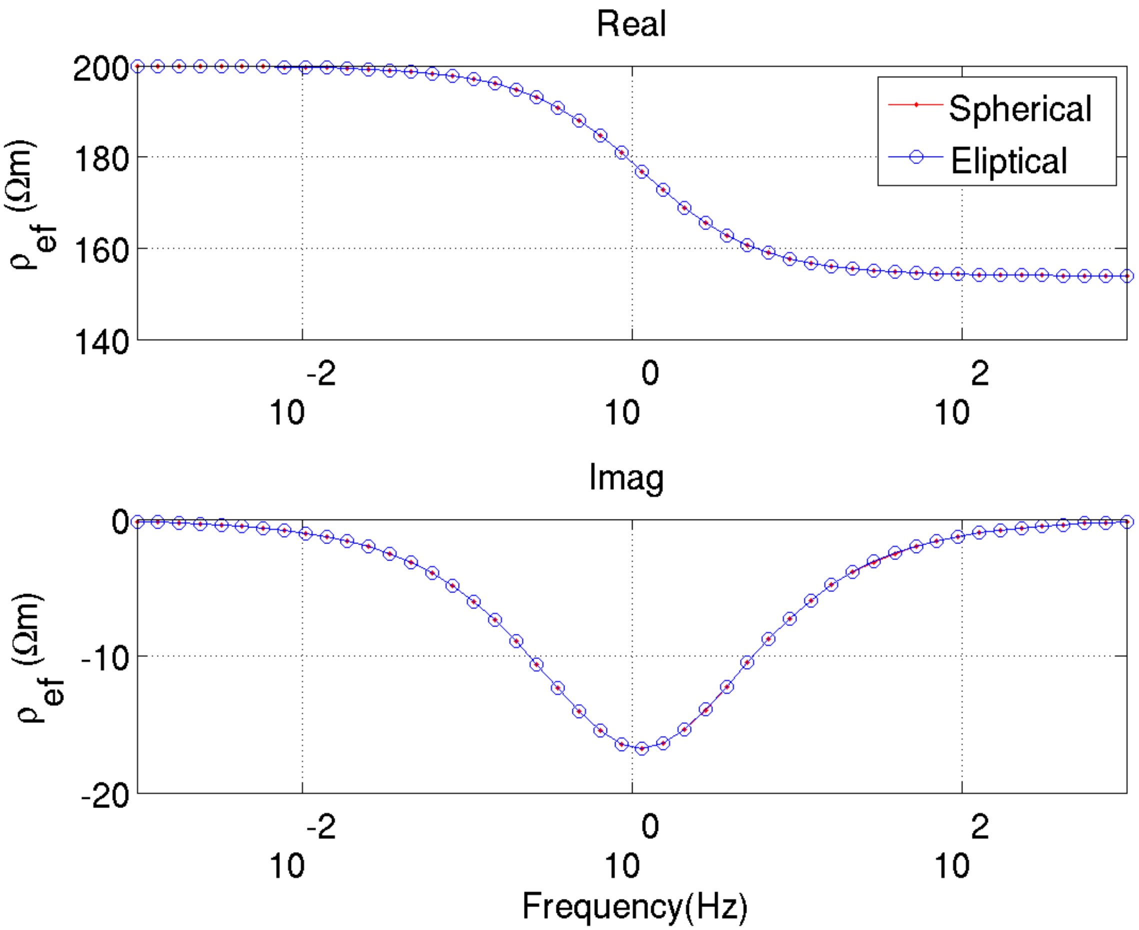

Figure 1.7. Comparison of two-phases spherical model and two-phases ellipsoidal model while the ellipticity value equals 1.

CHAPTER 2

FORWARD MODELING AND INVERSION OF SYNTHETIC DATA

2.1 Forward modeling: GEMTIP model

Forward modeling using the GEMTIP resistivity model is an important step in understanding how IP parameters relate to complex resistivity data. Right now, there exist two analytical GEMTIP models that are used for modeling rock resistivity. The first is called the spherical GEMTIP model, and the second is called the ellipsoidal GEMTIP model. Their use and purpose is identical apart from the elliptical model having the ability to consider inclusion shapes of arbitrary ellipticity, using three different radius values. Spherical GEMTIP model was studied previously by Phillips (2010). In this paper, two-phases ellipsoidal GEMTIP model forward modeling was tested by varying parameters. Several synthetic models have been created to show how the parameters of ellipsoidal GEMTIP model affect real and imaginary resistivity data. In particular, I focused on modeling the effects of ellipticity (e), volume fraction (f), relaxation parameter (C), time constant (τ) and DC resistivity (ρ_0).

To understand in more detail what affect the different IP parameters within the GEMTIP model has on synthetic data, a series of scenarios, shown in Table 2.1 through Table 2.3, have been modeled.

Table 2.1 GEMTIP parameters used when varying ellipticity (e)

Parameter	Value
ρ_0 (Ωm)	50
f (%)	10
C	0.5
τ (s)	0.5
e	0.125, 0.25, 1, 4, 8

Table 2.2 GEMTIP parameters used when varying volume fraction (f)

Parameter	Value
ρ_0 (Ωm)	50
C	0.5
τ (s)	0.5
e	4
f (%)	1, 4, 6, 8, 10

Table 2.3 GEMTIP parameters used when varying relaxation parameters (C)

Parameter	Value
ρ_0 (Ωm)	50
τ (s)	0.5
e	4
f (%)	10
C	0.01,0.1,0.3,0.6,0.9

at Table 2.4 shows the GEMTIP parameters used when varying time constant (τ) from 0.001 to 10 at five different values while keeping other parameters the same. Table 2.5 shows the GEMTIP parameters used when varying resistivity (ρ_0) at five different values while keeping other parameters the same.

Figure 2.1 shows the GEMTIP resistivity model plotted, keeping all parameters constant but the ellipticity. In this example, five different values of ellipticity are chosen

Table 2.4 GEMTIP parameters used when varying time constant (τ)

Parameter	Value
ρ_0 (Ωm)	50
e	4
f (%)	10
C	0.5
τ (s)	0.001,0.01,0.1,1,10

Table 2.5. GEMTIP parameters used when varying resistivity (ρ_0)

Parameter	Value
e	4
f (%)	10
C	0.5
τ (s)	0.5
ρ_0 (Ωm)	50,100,200,400,500

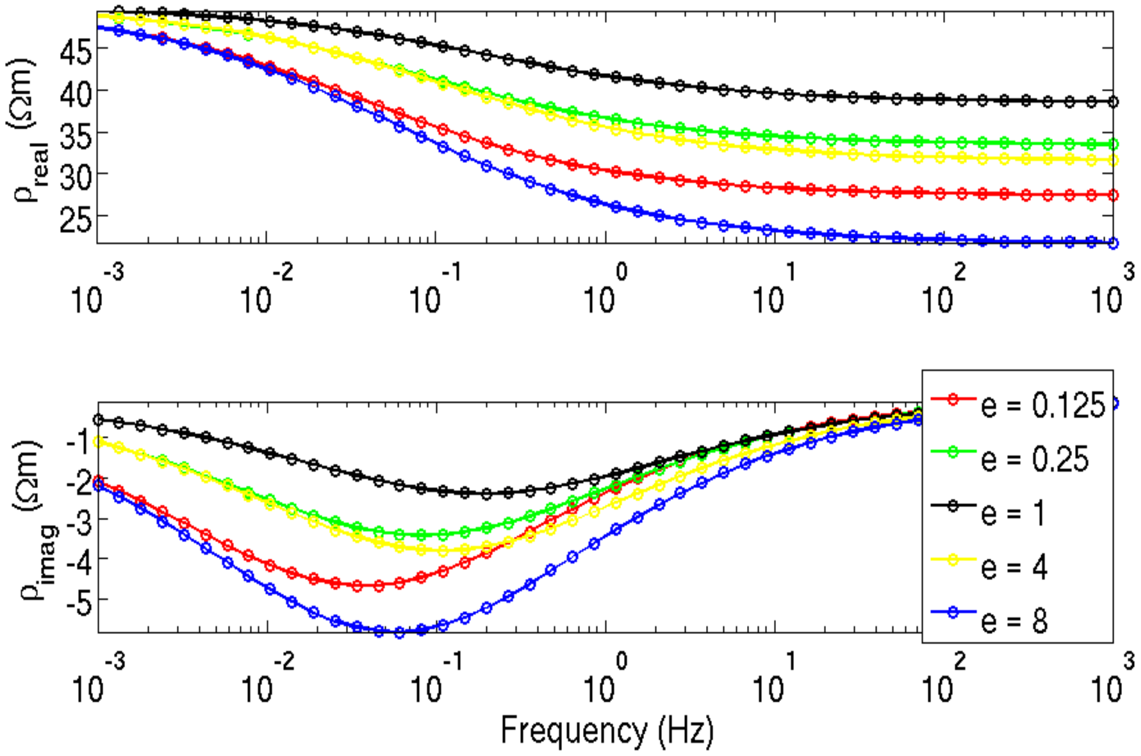

Figure 2.1. Ellipsoidal GEMTIP resistivity response obtained by keeping all parameters constant but changing the ellipticity (e).

to represent the range of reasonable values. It is very clearly shown that by varying e, the response of the computed resistivity shifts in frequency. Ellipticity e=1 represents the spherical GEMTIP model, e=0.125 and e=0.25 represent the oblate spheroid, while e=4 and e=8 represent the prolate spheroid. The result show the model is very sensitive to the ellipticity. Both oblate and prolate spheroid model show the lower frequency of maximum IP effect response than the spherical model has. For the oblate spheroid model, lower value of ellipticity has lower frequency of maximum IP. For the prolate spheroid model, higher value of ellipticity has lower frequency of maximum IP. Compare the results, the oblate spheroid model is more sensitive than the prolate spheroid model with the same gradient.

In this paper, I focus on the elliptical model study. In all other forward modeling, the value of e is 4. Figure 2.2 shows how varying the volume fraction (f) affects the computed resistivity values while holding all other parameters constant. From the model result, f appears to affect both the location of the resistivity response (in frequency) as well as its amplitude (both real and imaginary). By increasing f from 1% to 10%, it becomes clear that the amplitude of the resistivity response significantly decreases in the real and increases in the imaginary. Higher volume fraction will lead to lower frequency of maximum IP response. Understanding the effects of the volume fraction is particularly significant because it is one of the parameters that can be measured directly in lab.

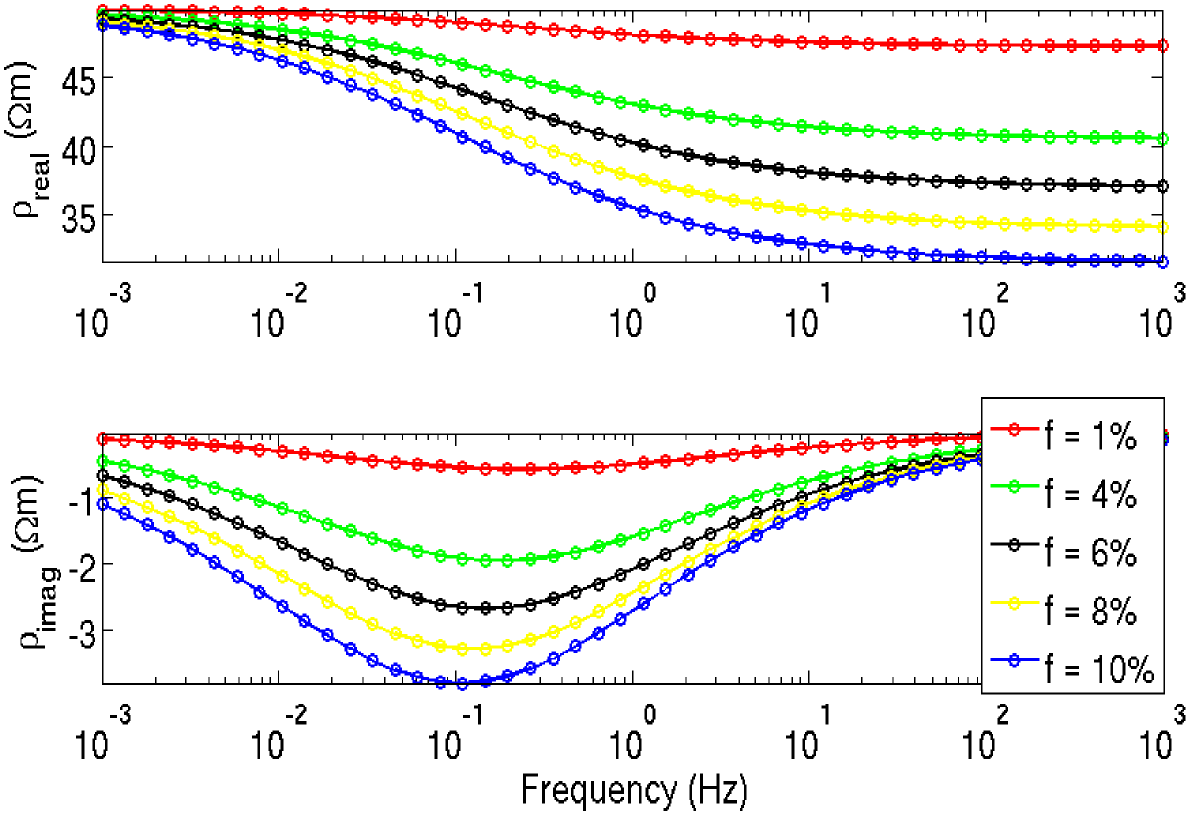

Figure 2.2. Ellipsoidal GEMTIP resistivity response obtained by keeping all parameters constant but changing the volume fraction (f).

Figure 2.3 shows how varying the relaxation parameter (C) affects the computed complex resistivity values while holding all other parameters constant. C appears to affect amplitude of resistivity for both real and imaginary resistivity. Typical values for C range from 0 to 1. Laboratory studies (Pelton, 1978) of IP have suggested that the relaxation parameter is not equal to 1. In contrast, high values of C tend to cause a dramatic decrease of resistivity in the real and cause a sharp resistivity peak in the imaginary.

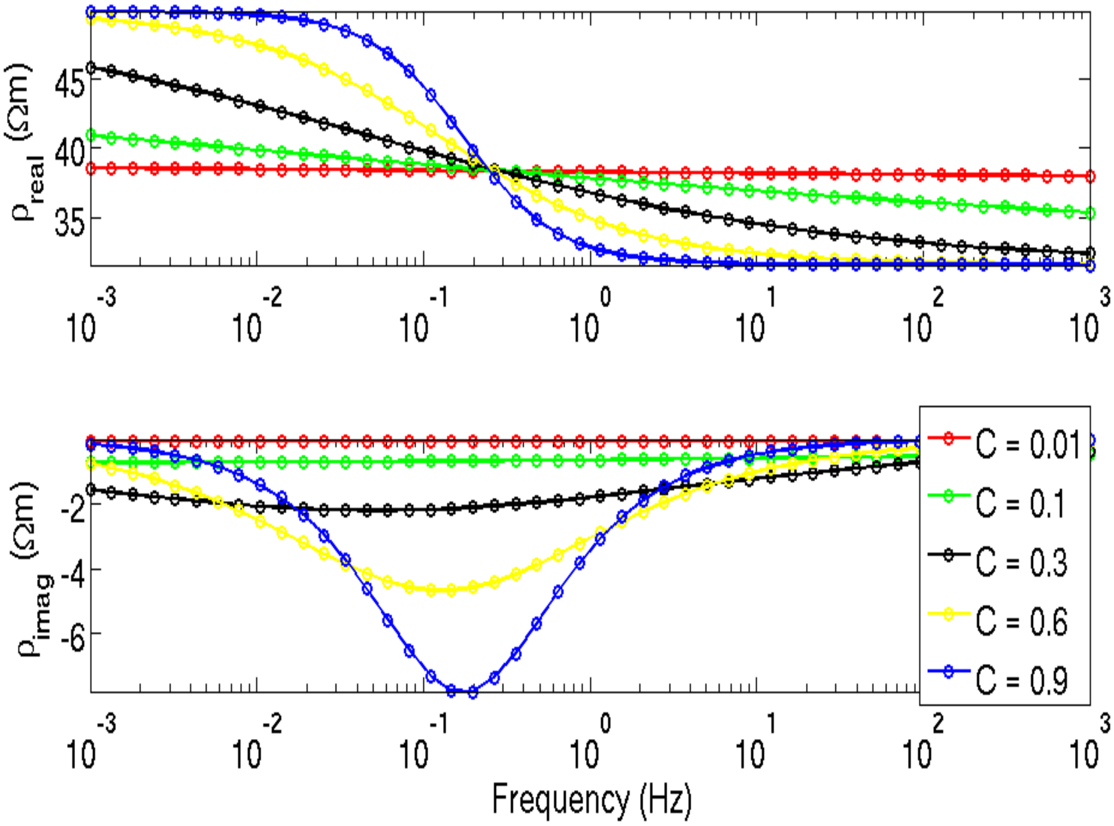

Figure 2.3. Ellipsoidal GEMTIP resistivity response obtained by keeping all parameters constant but changing the relaxation parameter (C).

Figure 2.4 shows how varying the time constant (τ) affects the computed complex resistivity values while holding all other parameters constant. The variability of time constant will change the amplitude in the real part and frequency location of maximum IP effect in the imaginary part. Higher time constant will have small real resistivity and lower frequency of maximum of IP effect. Emond (2007) showed that decreasing the grain size was analogous to decreasing the time parameter, which causes the maximum IP effect to be at a lower frequency.

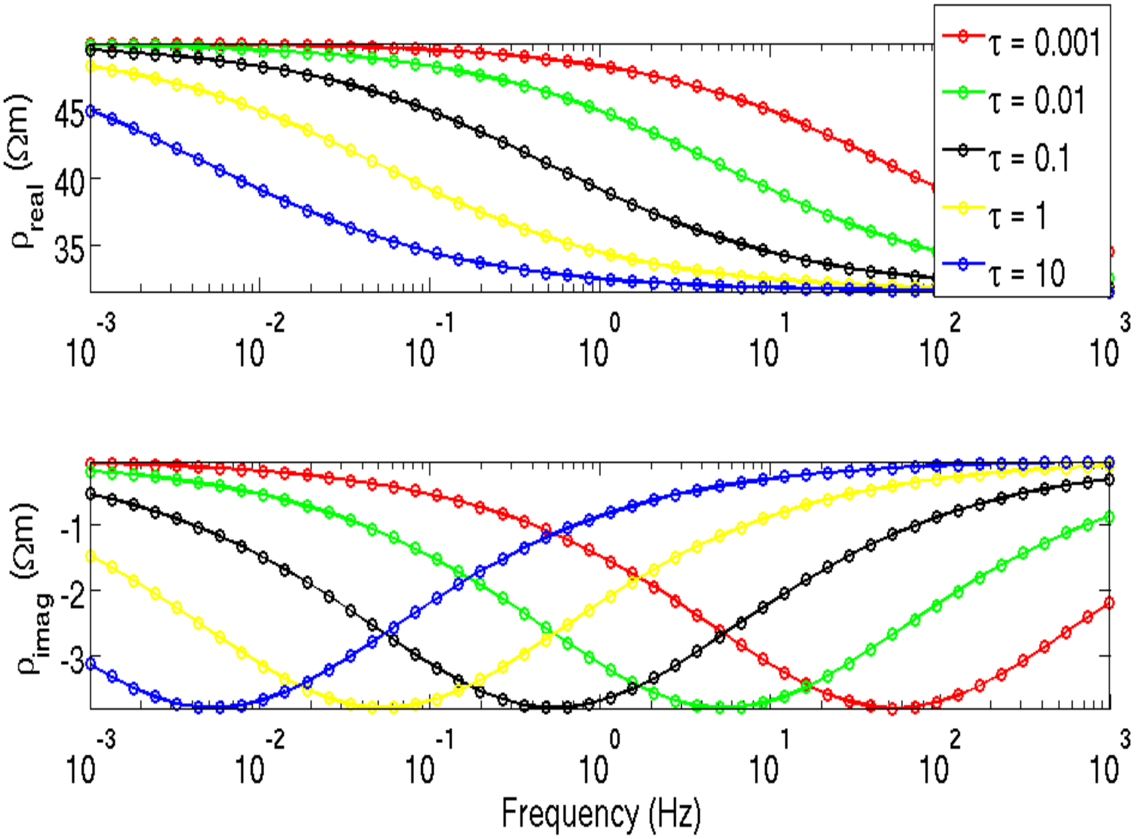

Figure 2.4. Ellipsoidal GEMTIP resistivity response obtained by keeping all parameters constant but changing the time constant (τ).

Figure 2.5 shows how varying the matrix resistivity (ρ_0) affects the computed complex resistivity values while holding all other parameters constant. It is very clear that the matrix resistivity affect both the real and imaginary amplitude directly. Higher resistivity corresponds to higher amplitude in both the real and imaginary resistivity curve. Further, it can not change the frequency of maximum of IP effect.

To sum up, for the randomly oriented ellipsoidal GEMTIP model, parameter ρ_0 and parameter C will affect the amplitude, parameter τ will affect the location of frequency of maximum IP effect, parameter f and parameter e will affect amplitude and frequency of maximum of IP effect. This result happened by changing only one GEMTIP

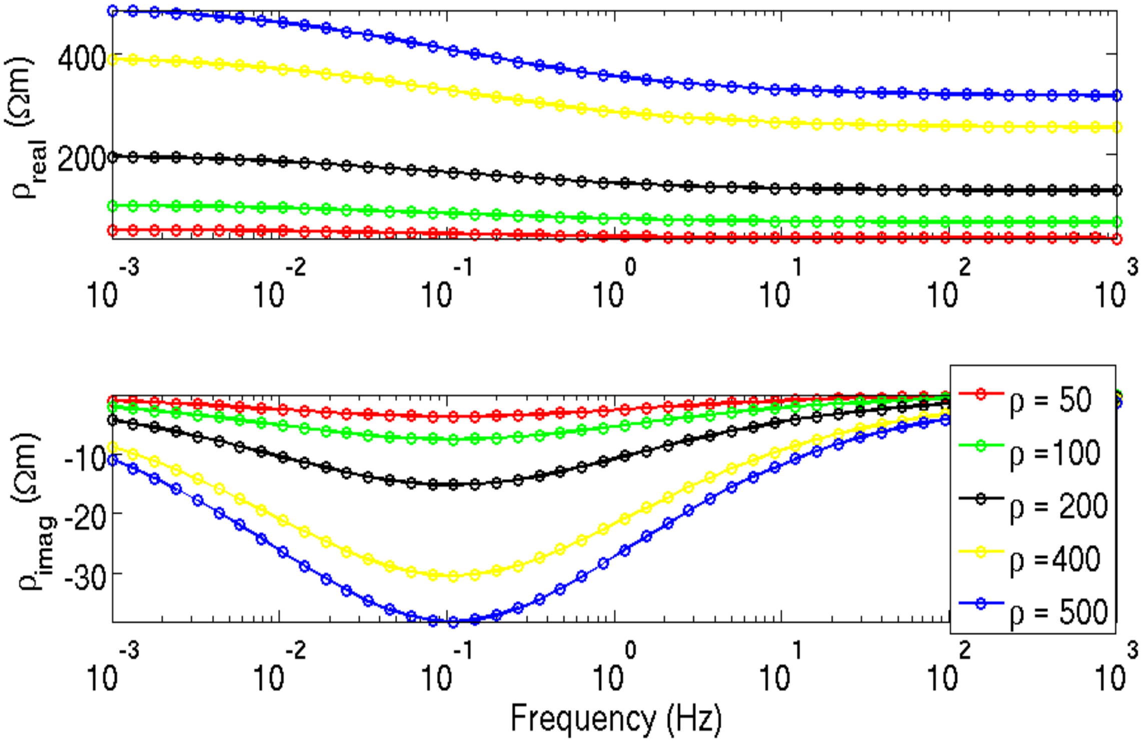

Figure 2.5. Ellipsoidal GEMTIP resistivity response obtained by keeping all parameters constant but changing the DC resistivity (ρ_0).

parameter while keeping the others constant. From the forward modeling study, it is found that the imaginary resistivity has the biggest change when changing parameters. That is why we can calculate the model parameter based on the imaginary resistivity data only.

2.2 Regularized conjugate gradient method

The purpose of inversion is to recover model parameters from measured data. An inverse problem can be formulated as the solution of the operator equation:

$$\mathbf{d} = \mathrm{A}(\mathbf{m}) \tag{2.1}$$

where $\mathbf{m}$ is some function (or vector) describing the model parameters, $\mathbf{d}$ is the data set and $\mathrm{A}(\mathbf{m})$ is the operator of forward modeling.

The problems in this research are ill-posed and unstable. To find the stable solution for the minimization problem, we have to consider the regularized minimization of the Tikhonov parametric functional:

$$P^{\alpha}(\mathbf{m}) = \Phi_{\mathrm{D}}^{2}(\mathrm{A}(\mathbf{m}), \mathrm{d}) + \alpha \mathrm{s}(\mathbf{m}) = \min \tag{2.2}$$

where $\mathrm{s}(\mathbf{m})$ is some stabilizing functional. The regularization ensures that a unique and stable solution is obtained from the measured data. The Regularized Conjugate-Gradient (RCG) method is utilized in this research period. Derivations and numerical schemes of both methods can be found in Zhdanov (2002).

The RCG method is an iterative solver, which updates the model parameters on each iteration using conjugate gradient directions $\tilde{\mathrm{l}}^{\mathrm{a}}$, according to the following formula:

$$\mathbf{m}_{\mathrm{n}+1} = \mathbf{m}_{\mathrm{n}} + \delta\mathbf{m} = \mathbf{m}_{\mathrm{n}} - \tilde{\mathrm{k}}_{\mathrm{n}}^{\alpha}\tilde{\mathrm{l}}^{\alpha}(\mathbf{m}_{\mathrm{n}}) \tag{2.3}$$

First, the direction of regularized steepest ascent is used:

$$\tilde{\mathbf{l}}^{\alpha}(\mathbf{m}_0) = \mathbf{l}^{\alpha}(\mathbf{m}_0) \tag{2.4}$$

The next direction is a linear combination of the regularized steepest ascent in this step, and the conjugate gradient direction in the previous step:

$$\tilde{\mathbf{l}}^{\alpha}(\mathbf{m}_1) = \mathbf{l}^{\alpha}(\mathbf{m}_1) + \beta_1^{\alpha}\tilde{\mathbf{l}}^{\alpha}(\mathbf{m}_0) \tag{2.5}$$

On the (n+1) step

$$\tilde{\mathbf{l}}^{\alpha}(\mathbf{m}_{n+1}) = \mathbf{l}^{\alpha}(\mathbf{m}_{n+1}) + \beta_{n+1}^{\alpha}\tilde{\mathbf{l}}^{\alpha}(\mathbf{m}_n) \tag{2.6}$$

The steps $\widetilde{k_n^a}$ are selected based on the minimization of the parametric functional:

$$P^{\alpha}(\mathbf{m}_{n+1}) = P^{\alpha}(\mathbf{m}_n) - \tilde{k}_n^{\alpha}\tilde{\mathbf{l}}^{\alpha}(\mathbf{m}_n) = \Phi(\tilde{k}_n^{\alpha}) \tag{2.7}$$

minimization of this functional gives the following best estimation for the length of the step using a linear line search:

$$k_n^a = \frac{(\widetilde{l_n^a}, l_n^a)}{(\widetilde{l_n^a}, F_{mn}^* F_{mn} + a(W * W)\widetilde{l_n^a})} = \frac{(\widetilde{l_n^a}, l_n^a)}{\left\|F_{mn}\widetilde{l_n^a}\right\|^2 + a\left\|W\widetilde{l_n^a}\right\|^2} \tag{2.8}$$

The β_n coefficients are determined by the following formula:

$$\beta_n^a = \|\mathbf{l}^a(\mathbf{m}_n)\|^2 / \|l^a(\mathbf{m}_{n-1})\|^2 \tag{2.9}$$

The final numerical scheme for the RCG method can be summarized as follows:

$$r_n = A(\mathbf{m}_n) - d \tag{2.10}$$

$$l_n^a = \widetilde{l_n^a}(\mathbf{m}_n) = F_{mn}^*\mathbf{r}_n + a(W * W)(\mathbf{m}_n - \mathbf{m}_{apr})$$

$$\beta_n^a = \|\mathbf{l}_n^a\|^2 / \|\mathbf{l}_{n-1}^a\|^2$$

$$\widetilde{\mathbf{l}_n^a} = \mathbf{l}_n^a + \beta_n^a \widetilde{l_{n-1}^a}$$

$$\tilde{l}_0^{\alpha} = l_0^{\alpha}$$

$$\widetilde{k_n^a} = (\widetilde{l_n^a}, l_n^a) / \left[\left\|F_{mn}\widetilde{l_n^a}\right\|^2 + a\left\|W\widetilde{l_n^a}\right\|^2\right]$$

$$m_{n+1} = m_n - \widetilde{k_n^a}\widetilde{l_n^a}$$

The initial regularization parameter α is calculated using the equation 2.11,

$$a = \frac{\|\mathrm{A}(\mathbf{m}_1) - \mathrm{d}\|^2}{\|\mathbf{m}_1 - \mathbf{m}_{\mathrm{apr}}\|^2} \tag{2.11}$$

We also implement the adaptive regularization, therefore, a_n becomes

$$\mathrm{a}_\mathrm{n} = \mathrm{a}\mathrm{q}^\mathrm{n} \tag{2.12}$$

where:

$$0 < \mathrm{q} < 1 \tag{2.13}$$

The iterative process is terminated when the misfit reaches the given level or the iterative number reaches the maximum.

$$\Phi(\mathbf{m}_\mathrm{n}) = \|\mathrm{r}_\mathrm{n}\|^2 \leq \varepsilon \tag{2.14}$$

In addition, I also used the extensive line search method in my study. The basic idea of this method has three steps. First, find all possible value ranges of the model parameters and determine $\mathrm{m}_{\mathrm{min}}$ and $\mathrm{m}_{\mathrm{max}}$ value; secondly, divide the possible parameter values and calculate misfit by using all possible parameters combinations; finally, find the minimum misfit value and determine the model parameters. Both numerical schemes have been implemented using a code written in MATLAB.

2.3 Inversion: synthetic data

2.3.1 Model 1: two-phases ellipsoidal GEMTIP model

The used synthetic data set is obtained considering one disseminated phase that occurs at one grain size. The spherical model has proven to offer good results in a previous study (Phillips, 2010). In this example, I focus on the randomly oriented ellipsoidal GEMTIP model, the grains of the inclusions are approximated in shape by a prolate spheroid. The value of ellipticity is 4. It comprises a rock matrix with the resistivity, 200Ωm. The volume fraction of pyrite in the sample is 10%. The known values of the relaxation parameter and time constant are 0.8 and 0.1, respectively. The equal radius of the approximated prolate spheroid is 1mm. All the parameters used in the two-phase synthetic model are summarized in Table 2.6. With these variables defined, the complex effective resistivity can be determined by two-phase spherical GEMTIP model. Figure 2.6 shows both the real effective resistivity and the imaginary effective resistivity plotted as a function of frequency. The two data sets shown are observed and predicted data. The observed data came from using the true model parameters value, while the predicted data were determined by minimizing the parametric functional using the regularized conjugated gradient method. It is obvious that the original observed data fit the predicted data very well. The panel (c) shows the plot of misfit against iteration number. After 100 iterations, the correct model parameters were recovered, the final misfit is 0.01%.

Table 2.6 GEMTIP two-phases synthetic data inversion result

Parameter	True model	Initial model	Two-phases
ρ_0 (Ωm)	200	200	-
e	4	4	-
f (%)	10	50	10
C	0.8	0.1	0.8
τ (s)	0.1	0.5	0.1

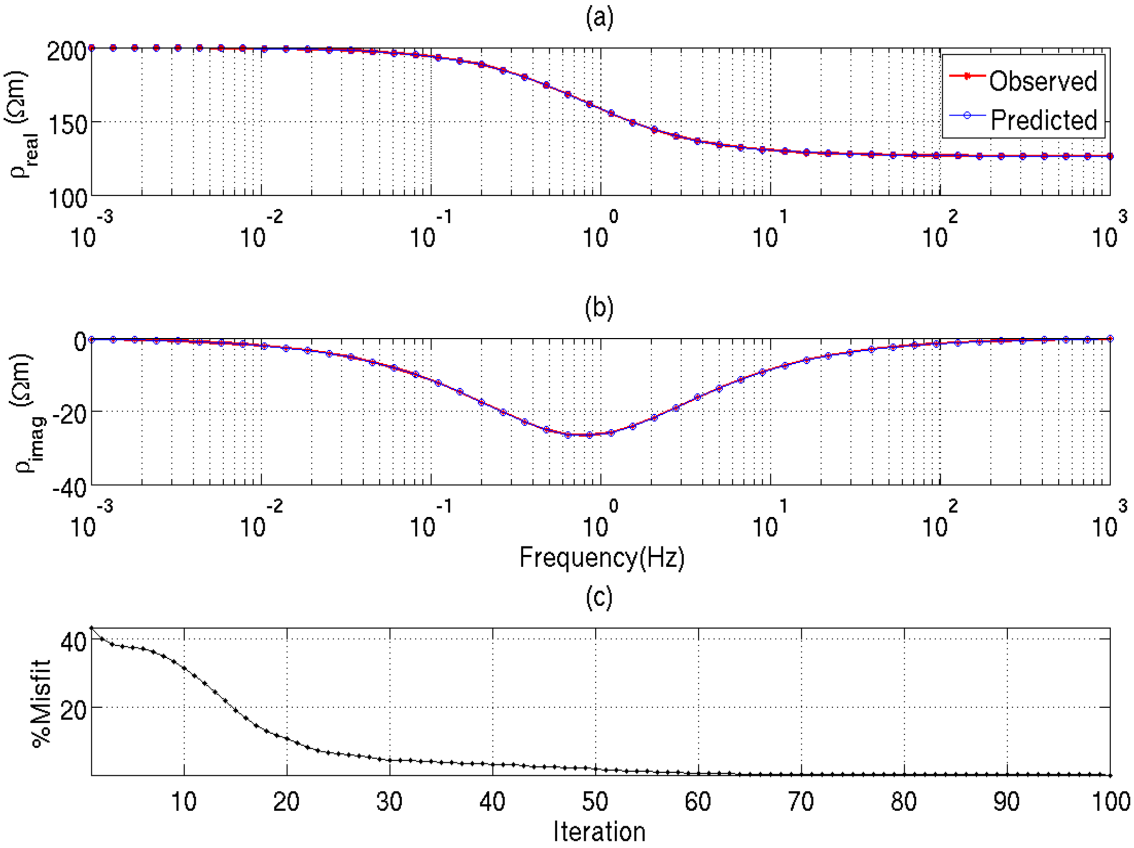

Figure 2.6. Two-phases synthetic data inversion result. (a) Real effective resistivity. (b) Imaginary effective resistivity. (c) Misfit vs. iteration.

2.3.2 Model 2: three-phases ellipsoidal GEMTIP model

Figure 2.7 represents both the observed and predicted resistivity curves for three-phases ellipsoidal GEMTIP model. The synthetic data are obtained from the forward modeling, considering a model formed by a homogeneous host rock filled with two types of grains and two grain sizes. All the parameters are summarized in Table 2.7. It clearly shows that there are two maximum IP responses in the imaginary part for the three-phases model. The observed curve came from using the true model parameter value, while the predicted data were obtained by minimizing the misfit functional using the extensive search method. The predicted data fit the original observed data very well. The final misfit is 0.3%.

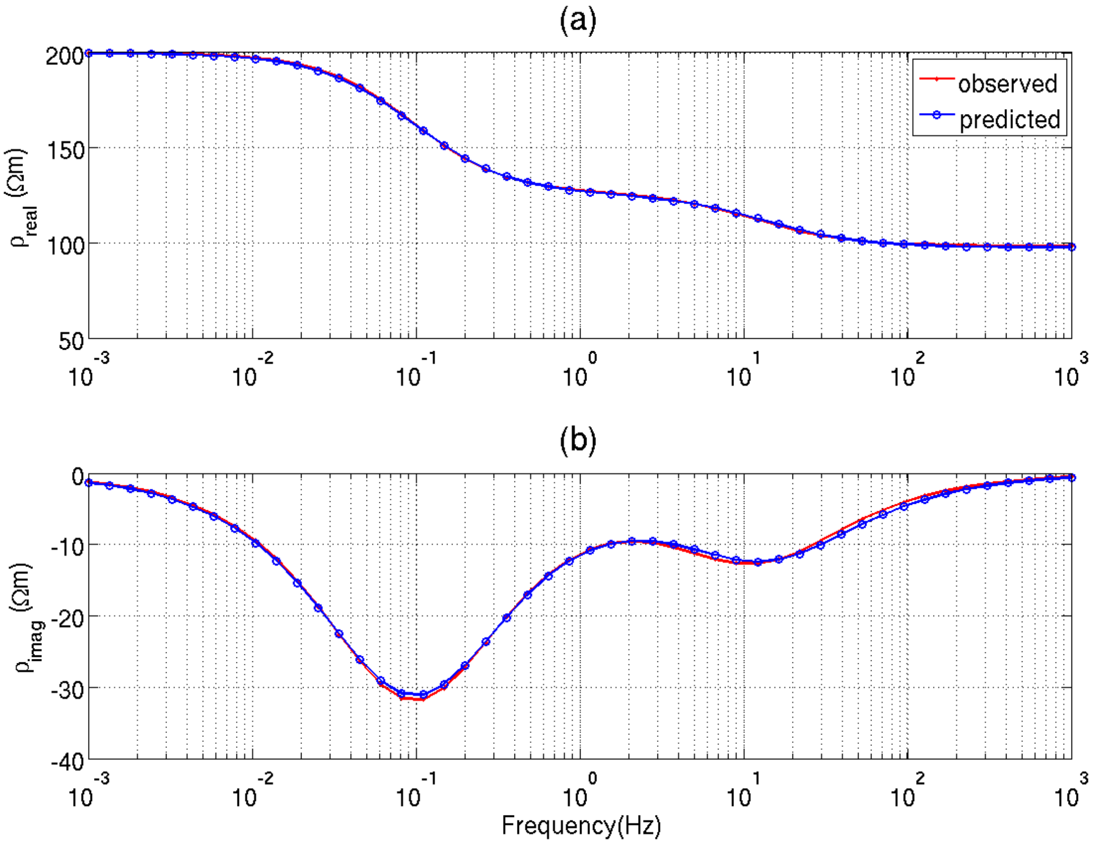

Figure 2.7. Three-phases synthetic data inversion result. (a) Real effective resistivity. (b) Imaginary effective resistivity.

Table 2.7 Three-phases synthetic data inversion result

Parameter	True model	Three-phases result	Three-phases with 5% noise result
$\rho_0(\Omega m)$	200	200	202
e_1	1	1	1.9
e_2	4	3.9	3.7
f_1 (%)	15	15	13
f_2 (%)	10	10	11
C_1	0.9	0.88	0.88
C_2	0.9	0.88	0.88
$\tau_1(s)$	0.01	0.009	0.009
τ_2 (s)	0.9	0.88	0.89

2.3.3 Model 3: three-phases ellipsoidal GEMTIP model with 5% random noise

Now I have added 5% random noise to the data while all the parameters are kept the same as in the previous three-phases synthetic model. The observed and predicted resistivity variations with frequency are illustrated in Figure 2.8. The recovered parameters are shown in Table 2.7. The final misfit is 4.3%. From the figure, the predicted curve fit the observed data very well. The comparison results between three-phases synthetic data and three phases synthetic data with noise are shown in Figure 2.9. From the synthetic data with noise study, I conclude that the inversion code is reliable for the work in the following chapter.

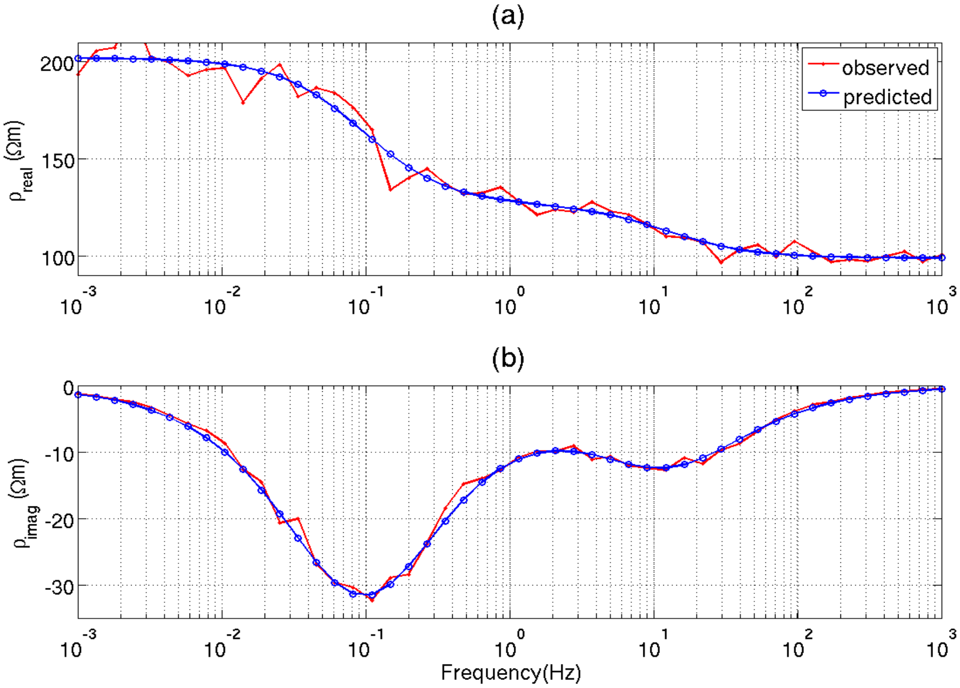

Figure 2.8. Three-phases synthetic sample with 5% noise inversion result. (a) Real effective resistivity. (b) Imaginary effective resistivity.

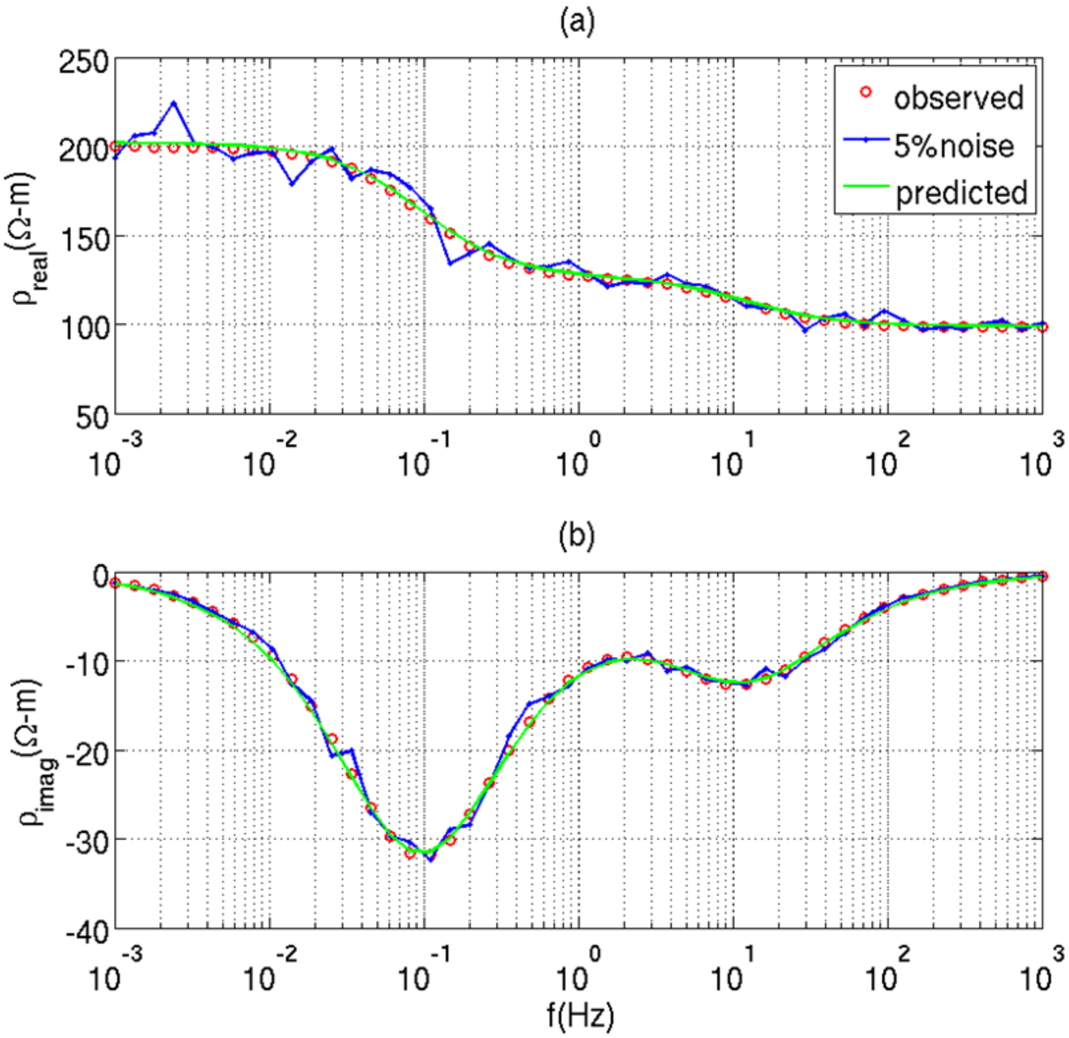

Figure 2.9. Comparison inversion result of three-phases synthetic data and three-phases synthetic data with 5% noise. (a) Real effective resistivity. (b) Imaginary effective resistivity.

CHAPTER 3

DATA ACQUISITION METHODOLOGY

This chapter analyzes the experimental data obtained for a representative set of rock samples. The ellipsoidal GEMTIP conductivity model was tested with two igneous and three shale rock samples. The two igneous samples were previously measured and studied by Fu (2011). The QEMSCAN images were obtained at the University of Utah, Department Geology and Geophysics. The complex resistivity data were measured at TechnoImaging in Salt Lake City in the USA. The sample description and data acquisition methodology will be made in this chapter.

3.1 Description of the samples

3.1.1 Igneous rock samples

Sample K01 is monzonite from the Kori Kollo mine in Bolivia with disseminated pyrite (FeS_2) and a predominantly sericite and quartz matrix. Picture of K01 is shown in Figure 3.1. This igneous rock was selected because of mineral inclusions that are potentially ideal for analysis by the GEMTIP rock physics model.

For better understanding of the three-dimensional (3D) structure and composition, sample K01 was analyzed using 3D X-ray microtomography (Burtman, 2008). The X-ray microtomography created a 3D volume of attenuation coefficients. The attenuation coeff-

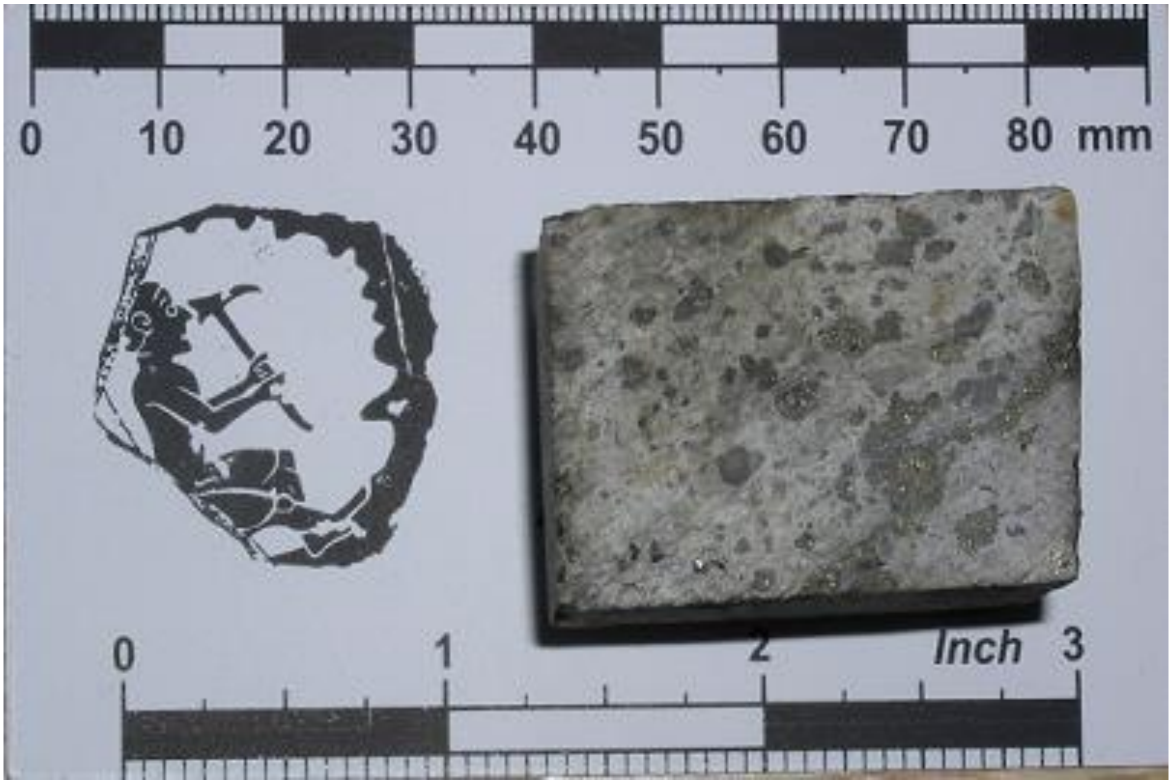

Figure 3.1. Sample K01. Monzonite from the Kori Kollo mine, Bolivia.

icients were used to distinguish the pyrite from the rock matrix. In addition to the 3D image, the volume fraction, inclusion size, and surface area can be determined by X-ray microtomography. For example, a 3D microtomographic image of sample K01 is shown in Figure 3.2, the image has been chosen to highlight the sulfide phases. A summary of the X-ray microtomography can be seen in Table 3.1.

Sample #13 is porphyry copper deposit from the mines at Sar Cheshmeh in Iran, which is the world's second largest lode of copper ore (5% of the world's total). This sa-

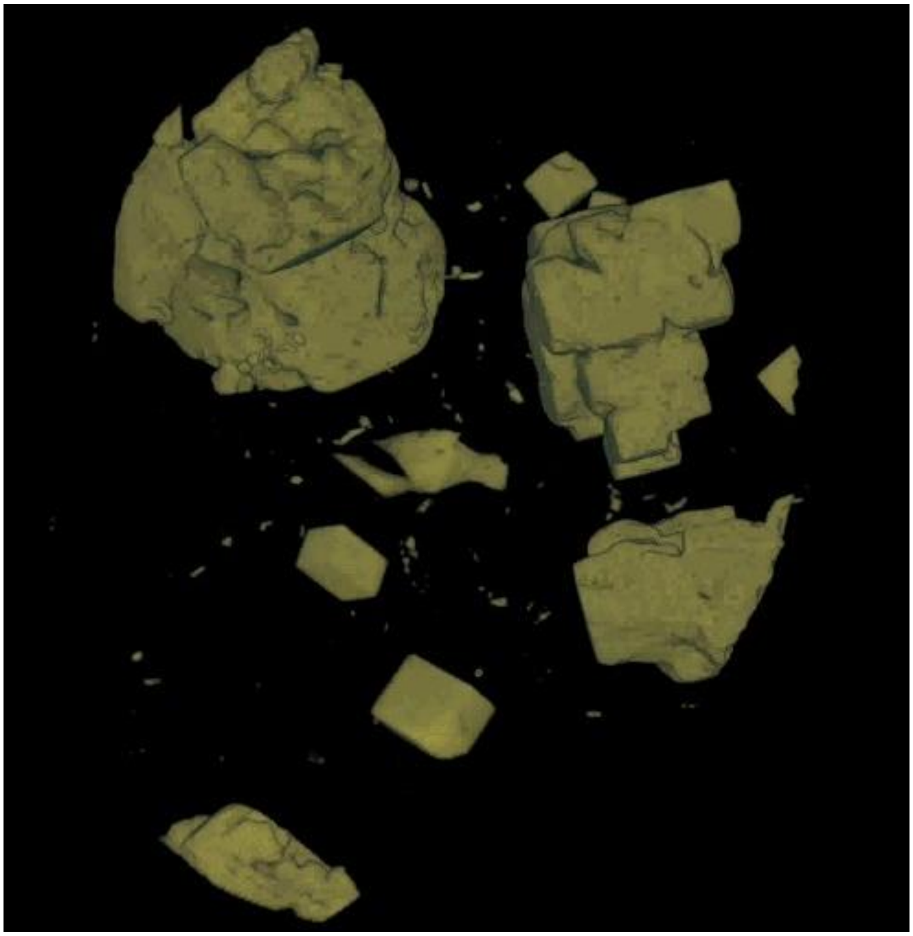

Figure 3.2. X-ray tomography image of Sample K01, Korri Kollo, Bolivia. The image has been optimized to show the pyrite.

Table 3.1 K01 mineralogical summary

Method	Matrix composition	Pyrite volume fraction	Pyrite radius
Optical	sericite, quartz	10%	1 to 2.5 mm
X-ray	quantitative	7%	478 inclusions. 90% volume from 0.5 to 1.3 mm.
X-ray	qualitative	-	predominantly 1 to 2 mm with smaller grains

mple contains disseminated chalcocite (Cu_2S), chalcopyrite ($CuFeS_2$), and pyrite (FeS_2) and a predominantly feldspar, quartz, and micas matrix. A picture of sample #13 is shown in Figure 3.3. The shiny spots are chalcopyrite and pyrite inclusions. All sulfides are introduced during vein formation (introduction of quartz). Later, during supergene enrichment chalcopyrite is partially replaced by chalcocite. Pyrite is not attacked by chalcocite. K-feldspar phenocrysts (green) are altered to muscovite. The rest of the rock consists of K-feldspar and quartz.

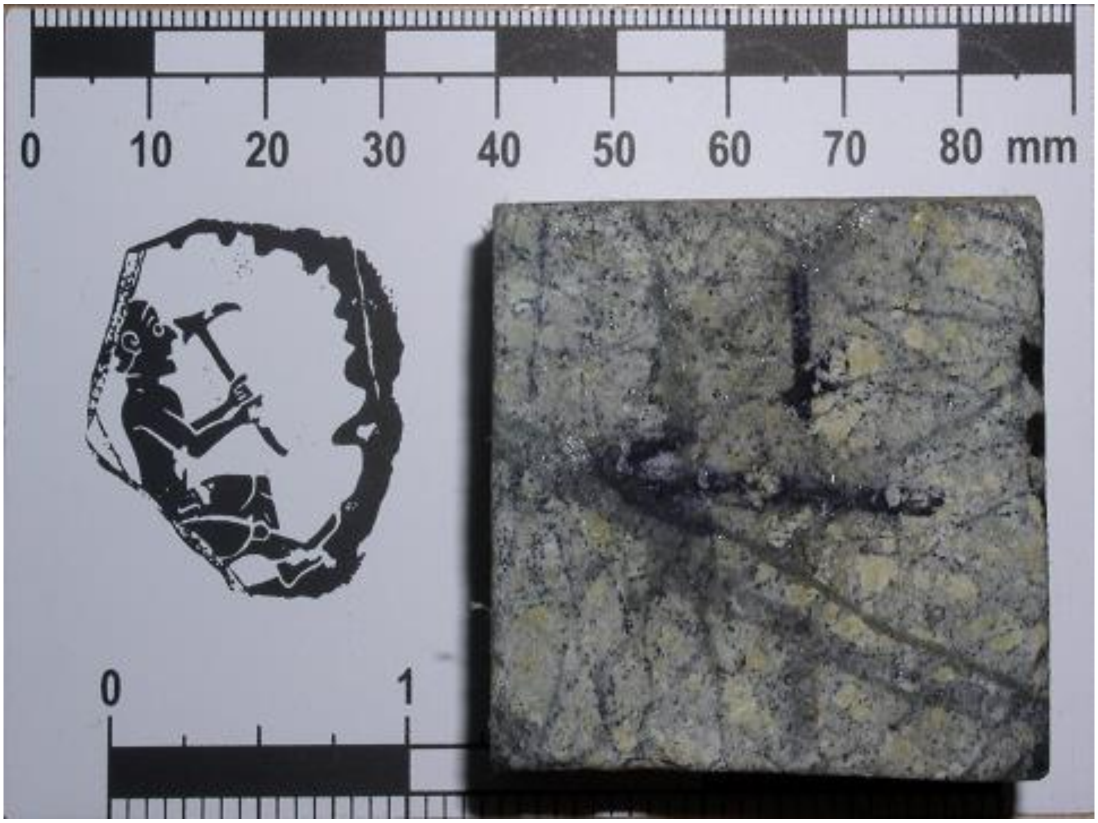

Figure 3.3. Sample #13. Porphyry copper deposit from Sarchesme, Iran with disseminated chalcocite (Cu_2S), chalcopyrite ($CuFeS_2$), and pyrite (FeS_2).

3.1.2 Shale samples

Three shale samples from Terratek were used in this study. The sample number is: #8, #33 and #45, respectively. The pictures of samples are shown in Figure 3.4. Sample #8 is a shale-oil sample, sample #33 is a shale-gas sample and sample #45 is a laminated shale-gas sample. X-ray diffraction data for whole rock and clay mineralogy by weight% is shown in Table 3.2. All the samples are rich in clay minerals, and also contain some disseminated pyrite.

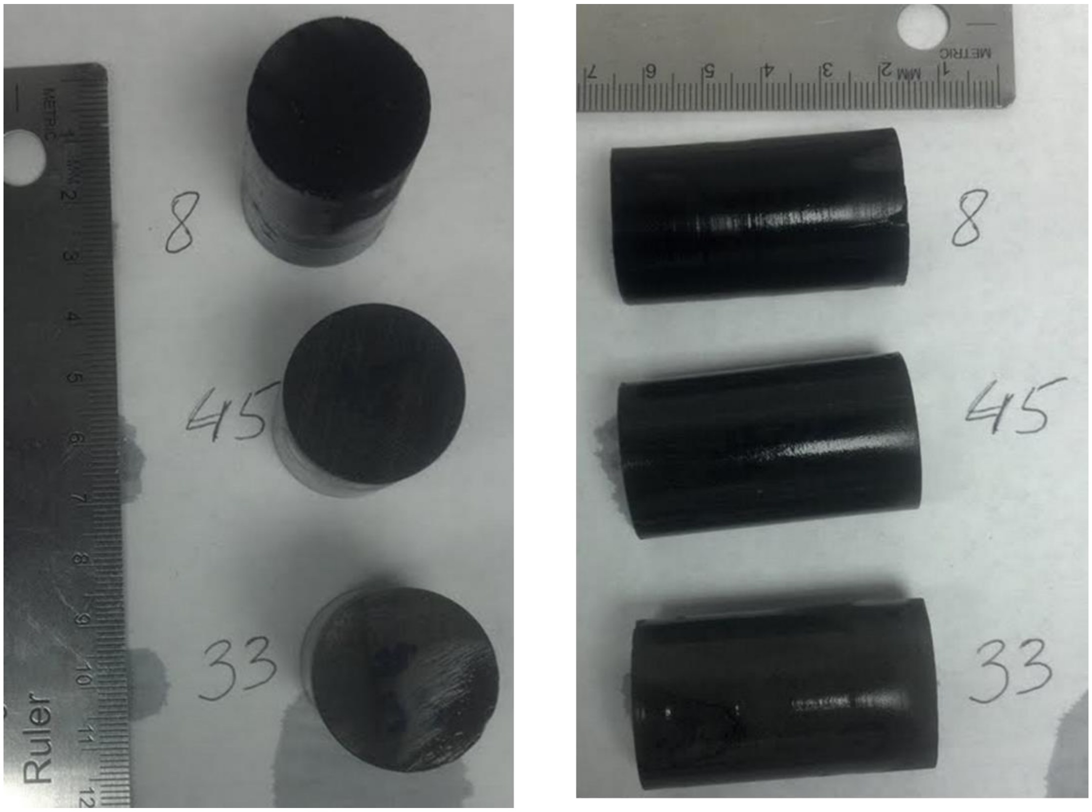

Figure 3.4. Terratek Sample. #8, shale-oil sample. #33, shale-gas sample. #45 laminated shale-gas sample.

Table 3.2 Sample mineralogy by X-ray diffraction (weight%)

	Sample ID	8	33	45
	Depth (ft)	8212.17	6197.4	13843.51
Whole Rock Mineralogy	Pyrite	4	0.5	2.6
	Quartz	23.8	2.7	18.4
	Calcite	10.3	93.3	50.4
	Ankerite/ Fe-dolomite	9.1	2.7	0.2
	Plagioclase	4.1	0	3
	K-feldspar	2.8	0	7.4
	Barite	0.7	0	0.4
	Dolomite	0	0.1	3.8
	Total nonclay	54.8	99.3	86.2
	Illite/Smectite (I/S)	5.8	0.6	2.1
	Illite+Mica	29.6	0	5.7
	Chlorite	8.3	0	3.5
	Kaolinite	1.6	0	2.5
	Total clay	45.3	0.6	13.8
Clay Mineralogy (<4 um)	Illite/Smectite (I/S)	48.8	49.6	32.9
	Illite	27	38.7	18.5
	% I/S expandability	25	20	20
	Chlorite	18	4.2	19
	Kaolinite	6	7.5	29.6
	Total clay	99.8	100	100

3.2 Sample preparation for complex resistivity analysis

3.2.1 Preparation for CR measurement

In order to use the shale samples for a laboratory experiment, special preparation procedures were required. First, each sample had to be trimmed to approximately 1 inch square to fit appropriately between the current electrodes. Second, if the sample was measured dry, the resistivity data collected would be meaningless, because the electrodes and the rock sample are not well contacted. Thus, in order for the electrolytes to flow through the porous volume of the sample, it had to be soaked in water for approximately 3 days before the measurement. This procedure was important because the soil had lost its field moisture. Additionally, the electrodes and the rock samples should be contacted in copper sulfate solution for about 10 minutes before starting the measurement. These two procedures were followed for each sample measured. In this study, #8, #33 and #45 were soaked in salt water for 5 to 8 days. The samples were saturated with the solution and isolated from the atmosphere in ziploc bags to reach and maintain equilibrium between the liquid and solid phase.

3.2.2 Preparation for QEMSCAN measurement

Each shale sample was prepared as standard polish thin sections in the lab, then carbon coated and submitted for measurement and analysis at University of Utah, Department of Geology and Geophysics. Figure 3.5 shows the sample thin section ready for QEMSCAN measurement. Figure 3.6 shows the setup for applying the carbon coat.

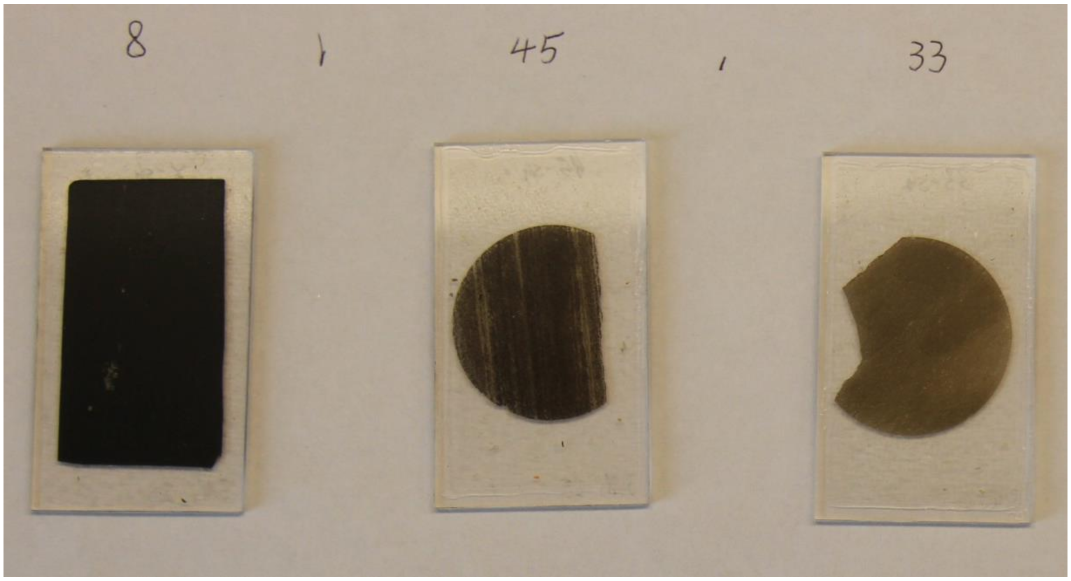

Figure 3.5. Sample thin section ready for QEMSCAN measurement.

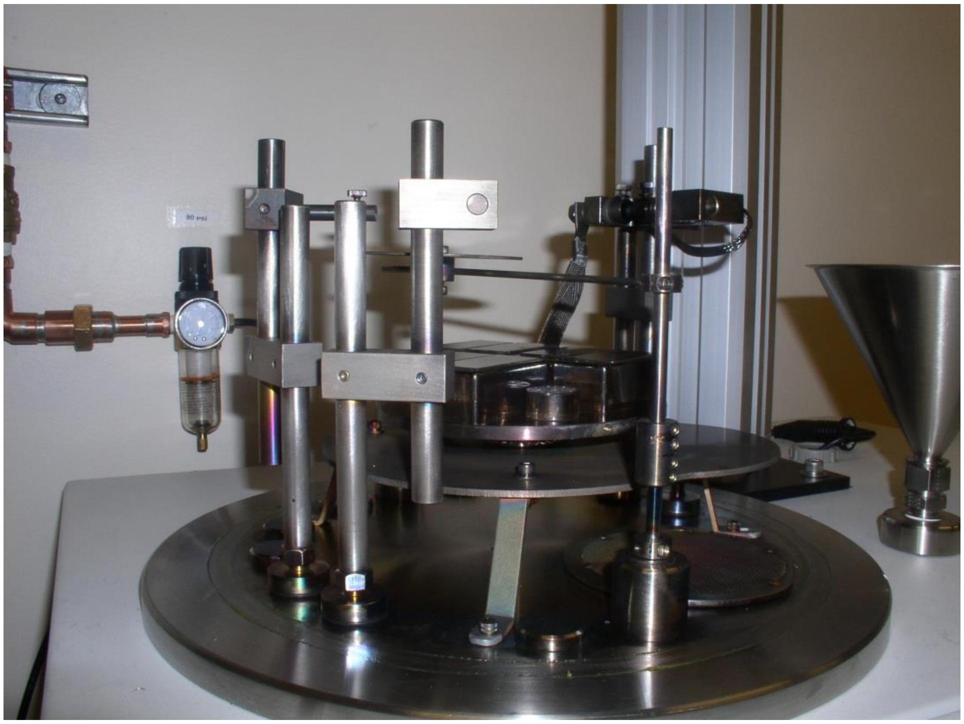

Figure 3.6. Setup of sample carbon coating.

3.3 QEMSCAN measurement

3.3.1 Principle of QEMSCAN Operation

QEMSCAN (Quantitative Evaluation of Minerals by Scanning Electron Microscopy) is the most powerful process mineralogical tool currently employed by the minerals industry. It is a fully-automated microanalysis system that enables quantitative chemical analysis of materials and generation of high-resolution mineral maps and images as well as porosity structure (Gottlieb et al., 2000). QEMSCAN is the fastest and most productive microbeam analysis system in the world, it uses a scanning electron microscopy platform (SEM) with an electron beam source in combination with four energy-dispersive X-ray spectrometers (EDS). A variety of quantitative information can be obtained including distribution, composition, and angularity of minerals, and the fabric, distribution, texture and porosity of materials. Figure 3.7 shows the component configuration of the QEMSCAN.

QEMSCAN measures particles or sections by collecting an individual EDX spectra and BSE (Backscatter Electron Intensity value), at every point on a grid. Each point is then individually identified as a phase or mineral using these data. Every pixel represents an individual measurement and mineralogical identification. The length of time for a full measurement will depend on the resolution of the measurement and the specific mineral. Figure 3.8 clearly shows how the minerals are identified by QEMSCAN. Each mineral is assigned a default false color that can be changed by the user. Analysis proceeds by collecting X-rays on spots arranged in a grid with a predetermined spacing within a small field of view. Sequentially analyzing and stitching together 1-3 mm size square fields yields an image of a portion or the entire surface of the sample. The resolu-

Figure 3.7. QEMSCAN component configuration at University of Utah, Department of Geology and Geophysics.

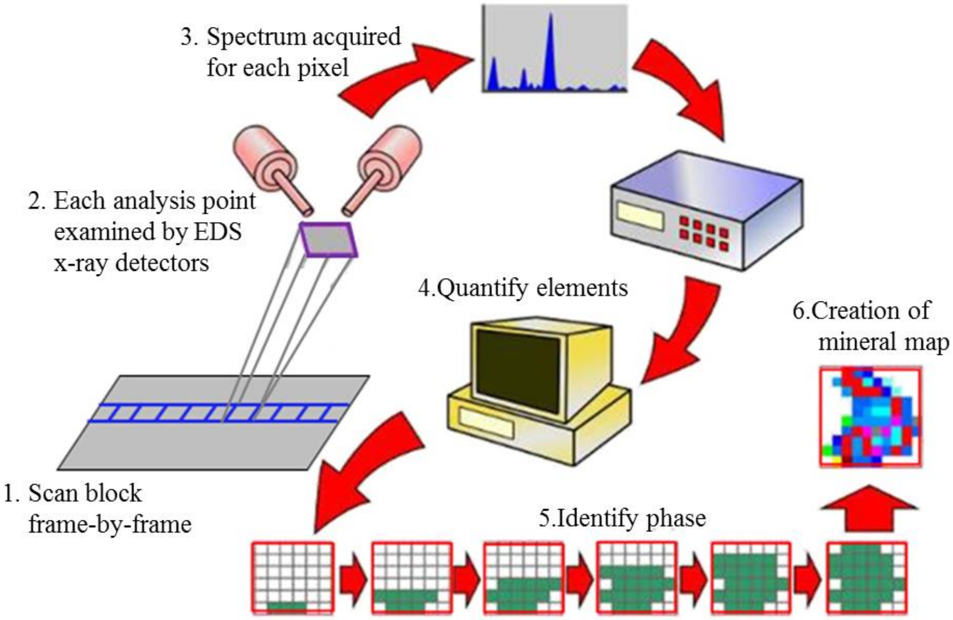

Figure 3.8. Schematic of how a QEMSCAN identifies minerals (modified from Training Manual, 2008).

tion of the image depends on the spacing of the analysis spots. The total length of time for an analysis depends on the total number of spots analyzed. The final result is an image that highlights the mineralogical aspect that the user seeks to convey. Analyses run in an automated fashion and run on a single sample may last a few minutes or many hours, depending on the experimental setup to obtain the required data. After the analytical run is complete, the results are examined and assembled into reports that focus on the users need. This involves the verification of the correct classification of spectra into relevant mineral grouping, color selection, generation of images and pertinent graphs and tables. Depending on the complexity of the sample this step can represent a significant portion of the entire analytical process. The QEMSCAN was operated using an accelerating voltage of 25kV and a specimen current of 5nA. For this study, the measurements were collected in field-scan mode, and X-ray data were collected every 5μm on the polished thin sections, total areas measured were 10mm^2 per sample, which equates to an analysis time of approximately 2 hours.

3.3.2 QEMSCAN data analysis

The analyses were completed at the University of Utah, Department of Geology and Geophysics, on a QEMSCAN 4300, which is built on a Zeiss Evo 50 SEM platform with four light element Bruker Xflash energy dispersive X-ray detectors. Energy-dispersive X-ray spectral analysis (EDX) involves the interpretation of secondary X-ray spectra to determine elemental composition, and ultimately, mineralogy. This instrument is currently testing beta versions of iMeasure v.4.3 software for the data acquisition, and iDiscover v.4.3 for the spectral interpretation and data processing. Terratek shale samples

(#8, #33, #45) and sample #13 have been analyzed using the QEMSCAN at the University of Utah, Department of Geology and Geophysics. A color coded map of mineral composition is created as well as a quantitative measurement of mineral abundance in area percent and inclusion size in micron. Figures 3.9, 3.10, 3.11 and 3.12 are a representative section of sample #8, #33, #45 and #13. The #8 contains 6.64% pyrite, 13.87% calcite, 7.54% quartz and 29.11% clay mineral (mica, feldspar, chlorite, kaolinite). The size of pyrite calculated by QEMSCAN is 10.21 microns; the #33 contains 1.41% pyrite, 95.41% calcite, and very small percent area of clay mineral. The size of pyrite calculated by QEMSCAN is 13.56 microns. The #45 contains 3.53% pyrite, 53.6% calcite, 10.99% quartz, and 5.56% clay mineral. The size of pyrite calculated by QEMSCAN is 12.39 microns. The sample #13 contains 3.61% chalcocite, 0.46% chalcopyrite, 0.38% pyrite, 0.02% pyrrhotite and 0.03% other sulphides, the size of sulphide is in the range from 20μm to 300μm. A summary of the QEMSCAN results can be seen in Table 3.3.

Table 3.3 Sample mineralogy by QEMSCAN

Sample	Mineral composition	Pyrite grain size
#8	6.64% pyrite, 13.87% calcite, 7.54% quartz	10.21 μm
#33	1.41% pyrite, 95.41% calcite	13.56 μm
#45	3.53% pyrite, 53.6% calcite, 10.99% quartz	12.39 μm
#13	3.61% chalcocite, 0.46% chalcopyrite 0.43% pyrite, 0.03% other sulphides	20 μm to 300 μm

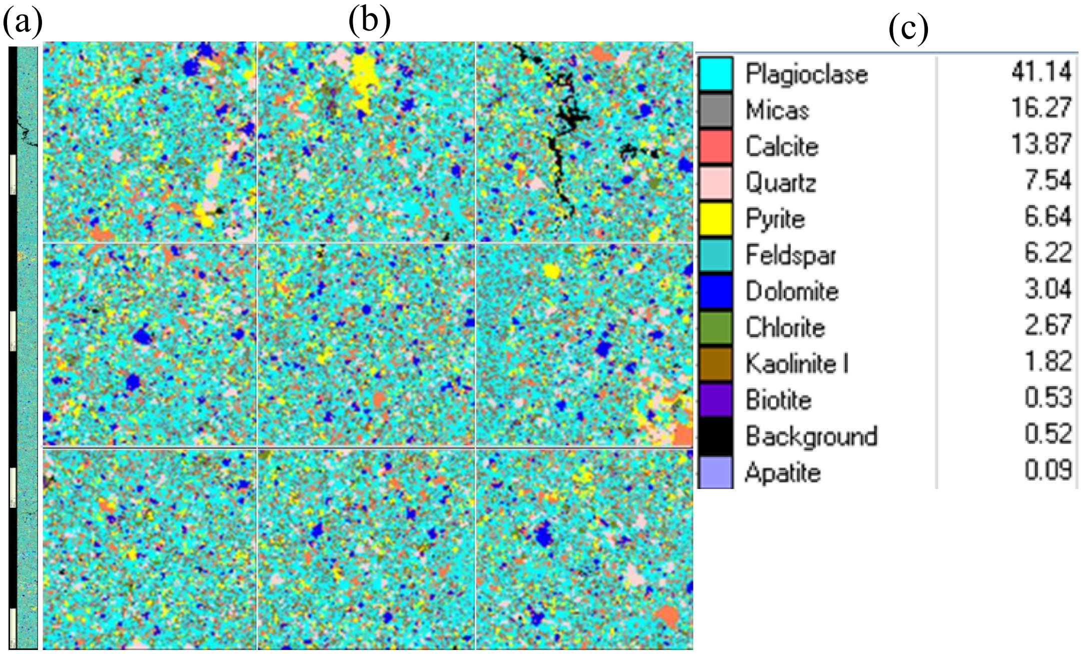

🟦	Plagioclase	41.14
⬜	Micas	16.27
🟥	Calcite	13.87
⬜	Quartz	7.54
🟨	Pyrite	6.64
🟦	Feldspar	6.22
🟦	Dolomite	3.04
🟩	Chlorite	2.67
🟫	Kaolinite I	1.82
🟪	Biotite	0.53
⬛	Background	0.52
🟦	Apatite	0.09

Figure 3.9. QEMSCAN results of sample #8. (a) The whole image of measured area. (b) The 9 field image (total field is 39). (c) Mineral name and area percent of the whole image.

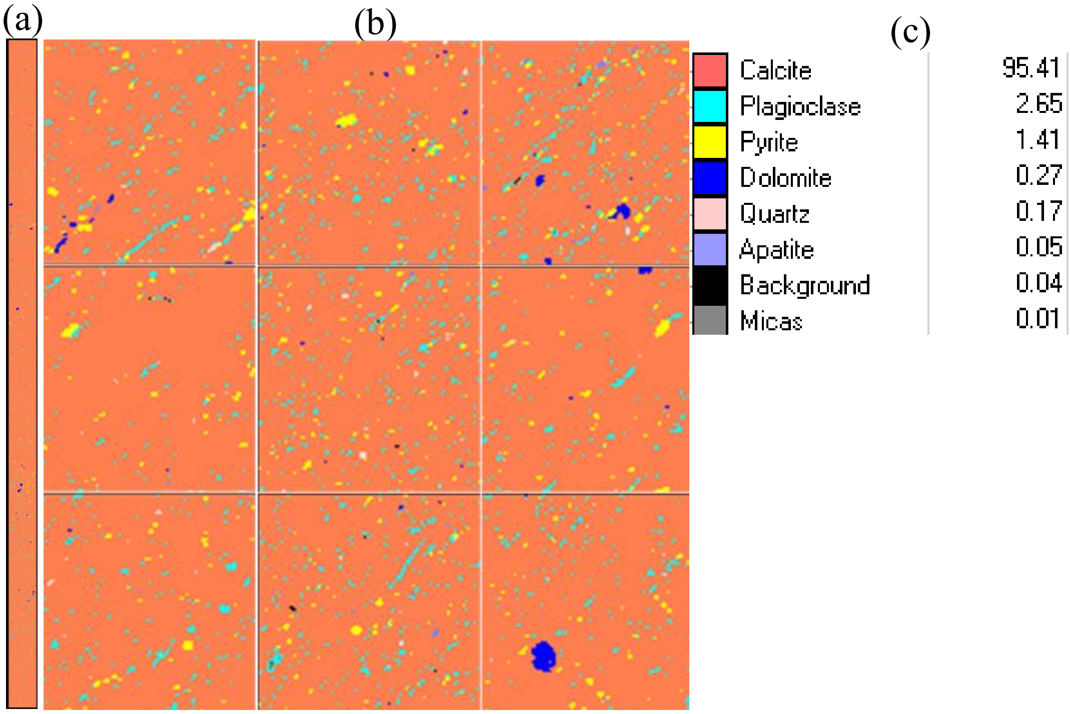

Calcite	95.41
Plagioclase	2.65
Pyrite	1.41
Dolomite	0.27
Quartz	0.17
Apatite	0.05
Background	0.04
Micas	0.01

Figure 3.10. QEMSCAN results of sample #33. (a) The whole image of measured area. (b) The 9 field image (total field is 39). (c) Mineral name and area percent of the whole image.

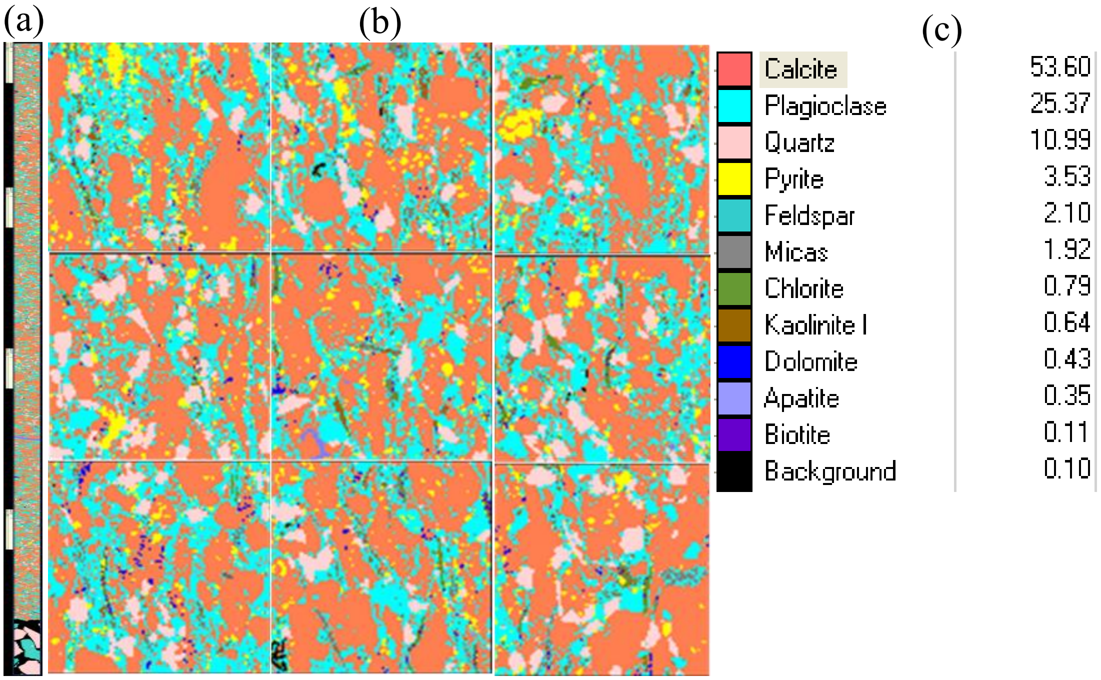

🟥	Calcite	53.60
🟦	Plagioclase	25.37
⬜	Quartz	10.99
🟨	Pyrite	3.53
🟦	Feldspar	2.10
■	Micas	1.92
🟩	Chlorite	0.79
🟫	Kaolinite I	0.64
🟦	Dolomite	0.43
🟪	Apatite	0.35
🟪	Biotite	0.11
⬛	Background	0.10

Figure 3.11. QEMSCAN results of sample #45. (a) The whole image of measured area. (b) The 9 field image (total field is 39). (c) Mineral name and area percent of the whole image.

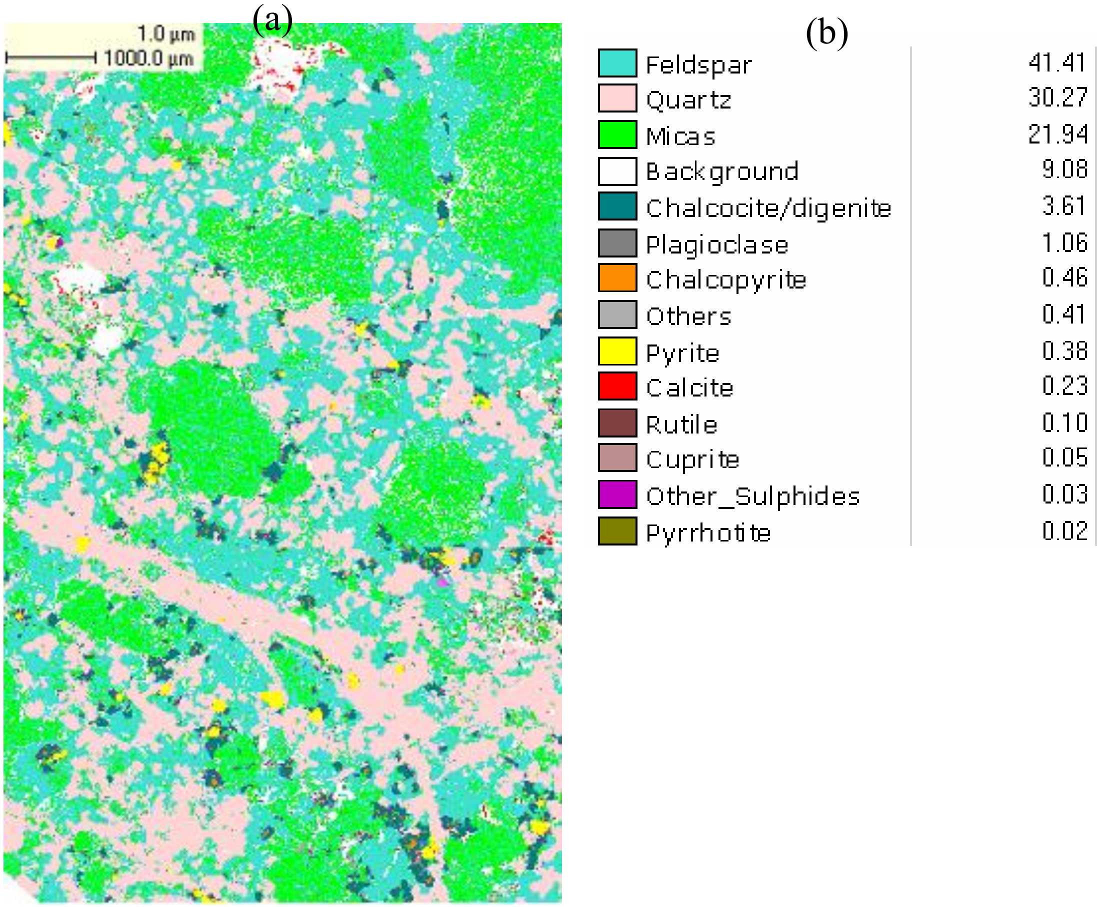

🟦	Feldspar	41.41
⬜	Quartz	30.27
🟩	Micas	21.94
⬜	Background	9.08
🟦	Chalcocite/digenite	3.61
⬛	Plagioclase	1.06
🟧	Chalcopyrite	0.46
⬜	Others	0.41
🟨	Pyrite	0.38
🟥	Calcite	0.23
🟫	Rutile	0.10
🟫	Cuprite	0.05
🟪	Other_Sulphides	0.03
🟫	Pyrrhotite	0.02

Figure 3.12. QEMSCAN results of sample #13. (a) The whole image of measured area. (b) Mineral name and area percent.

3.4 Complex resistivity measurement

Complex resistivity measurements were obtained from each sample at TechnoImaging. Frequency domain data were collected over a range (from about 0.005 Hz to about 10000 Hz) at 33 different frequencies. The equipment used to perform the measurement is shown in Figure 3.13.

Plots of the raw data recorded are shown in Figures 3.14, 3.15, 3.16, 3.17 and 3.18 for samples #8, #33, #45, K01, and #13. From the recorded data, we can clearly see one IP peak at low frequency (about 0.01~1Hz) in all samples, which were attributed by the disseminated sulphides, and the location of frequency of IP peak has the following rule: $\mathrm{f}_{\#33} < \mathrm{f}_{\#45} < \mathrm{f}_{\#8} < \mathrm{f}_{\#13} < \mathrm{f}_{\mathrm{K01}}$. In shale sample #45, we also can see another small IP peak located at 100Hz, that is caused by the membrane polarization. All shale samples should have the same properties in theory but do not, because the disseminated pyrite has enough concentration to show electrode polarization, the membrane polarization response can not be observed from the complex resistivity curve.

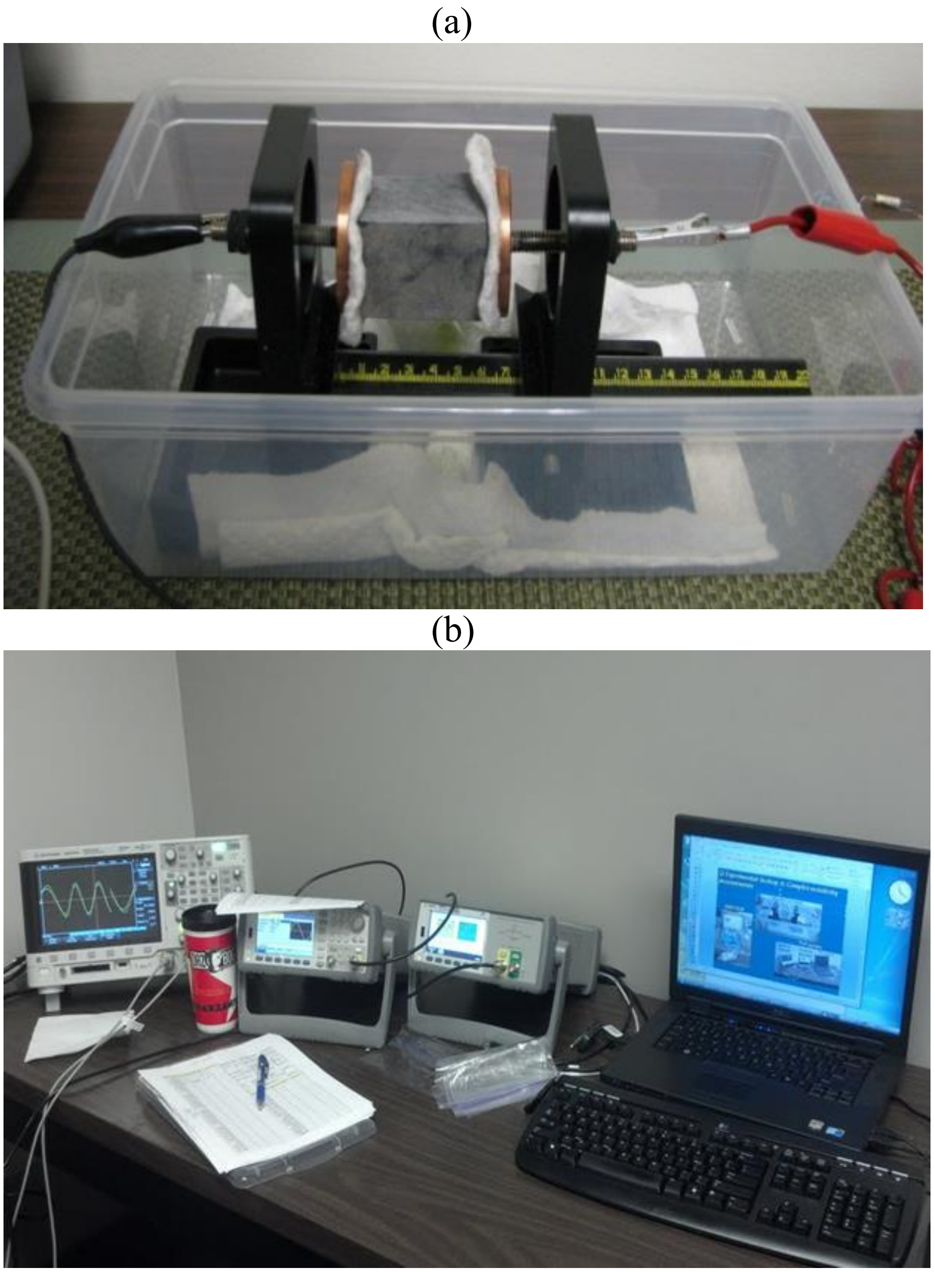

Figure 3.13. Recording system. (a) Sample holder, rock sample, receiving and transmitting electrodes. (b) Oscilloscope, waveform generator, isolation amp and computer.

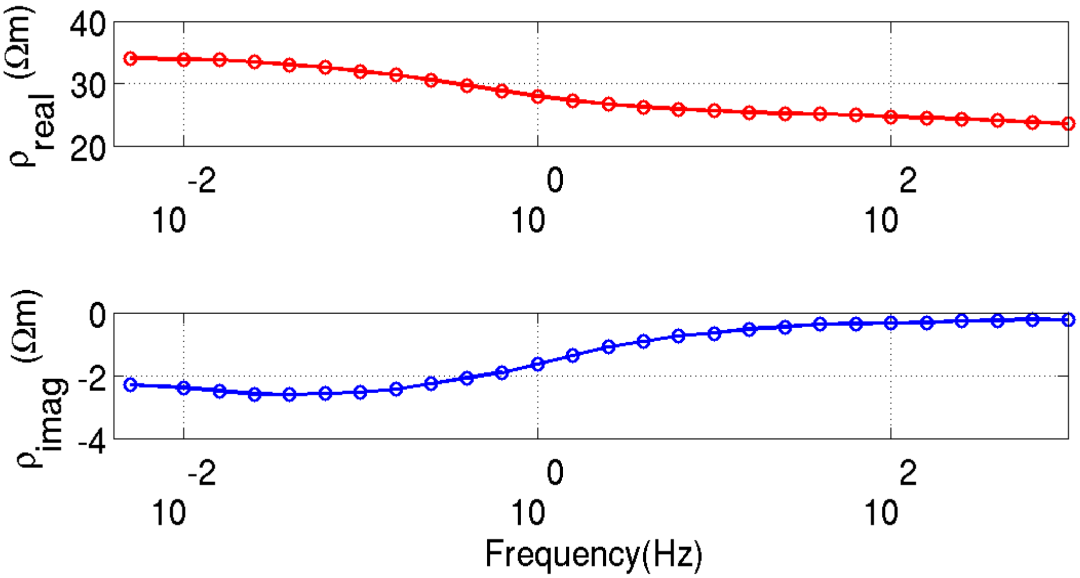

Figure 3.14. The plot of the resistivity data for sample #8.

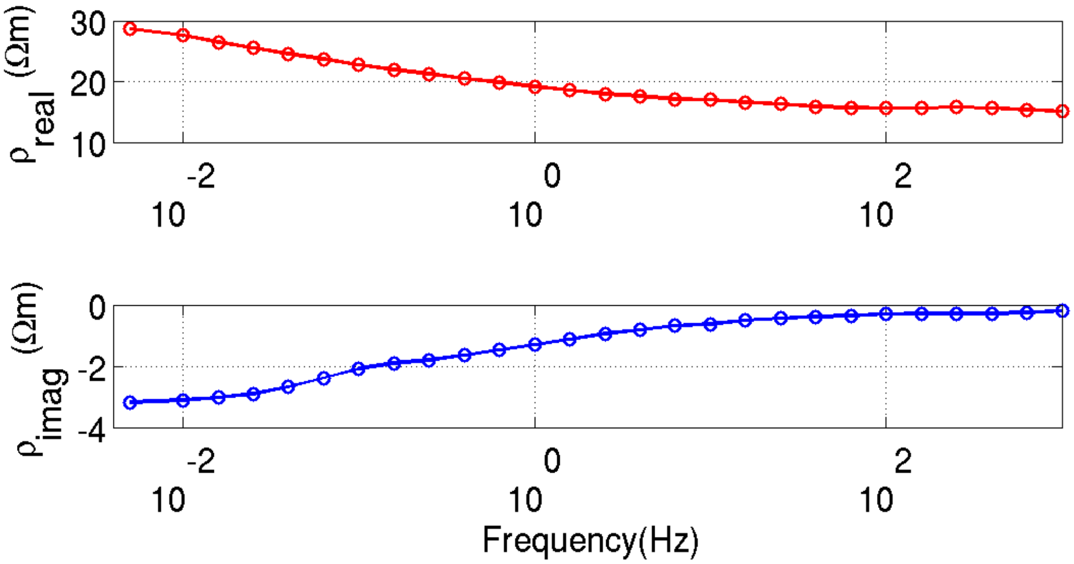

Figure 3.15. The plot of the resistivity data for sample #33.

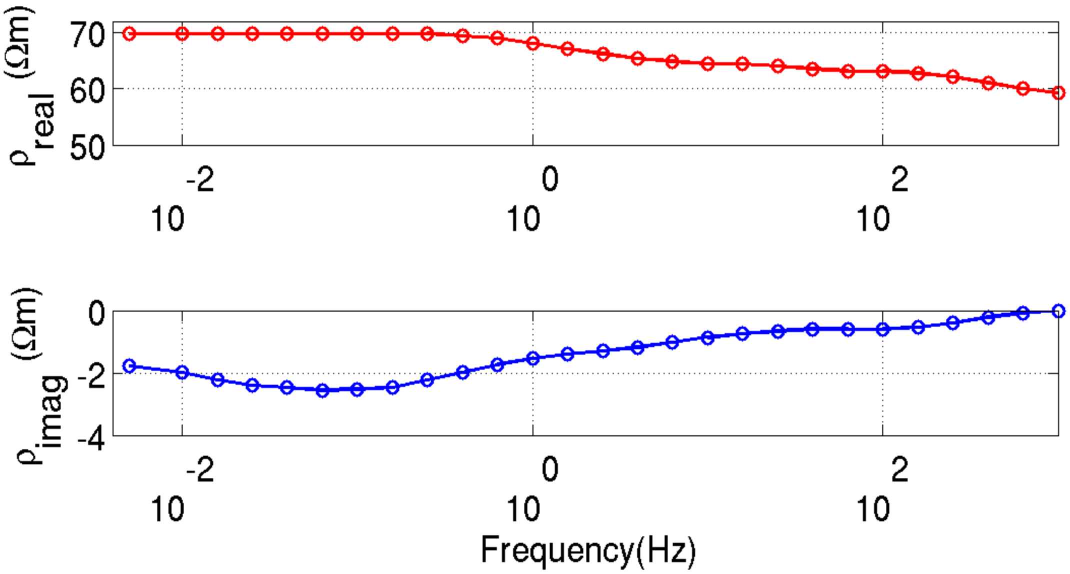

Figure 3.16. The plot of the resistivity data for sample #45.

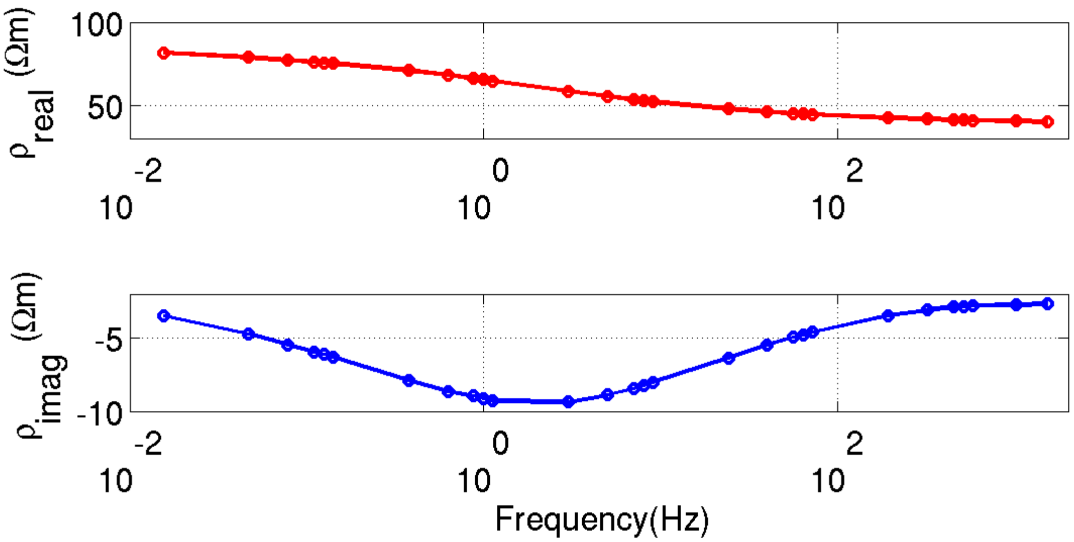

Figure 3.17. The plot of the resistivity data for sample K01.

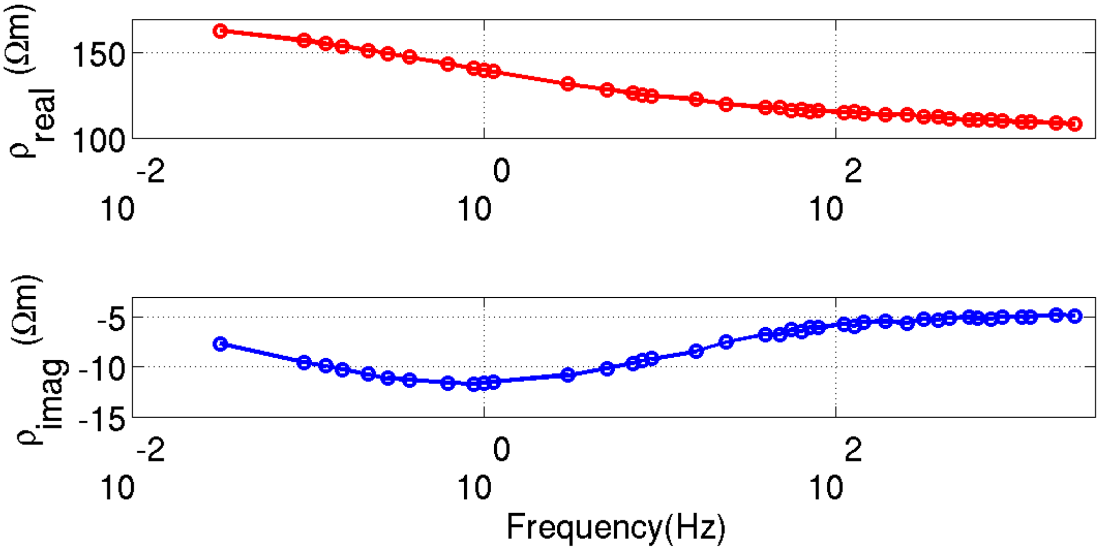

Figure 3.18. The plot of the resistivity data for sample #13.

CHAPTER 4

INVERSION RESULT

This chapter discusses the inversion results, which are based on the regularized conjugate gradient (RCG) method (Zhdanov, 2002) and extensive search method. The primary purpose is to invert the measured complex resistivity data for specific IP parameters. These parameters may be used practically to accurately discriminate minerals or predict useful geometric factors such as volume fraction. Additional information on these samples was extracted using the QEMSCAN and was used either as a priori information for the inversion, or as ground truth to which the inversion results could be compared. In my study, the RCG method was used in the two-phases ellipsoidal GEMTIP model, and the extensive search method was used in the three-phases ellipsoidal GEMTIP model. The RCG method inversion recovered parameters are volume fraction (f), relaxation parameter (C) and time constant (τ). While the extensive search method also invert matrix resistivity (ρ_0) and ellipticity (e).

4.1 Igneous rock samples

4.1.1 Sample K01

As previously mentioned, sample K01 is a monzonite from the Kori Kollo mine in Bolivia with disseminated pyrite and a predominantly sericite and quartz matrix. The diameter of the pyrite inclusions in this sample is a few millimeters. A previous study of sample K01, used the spherical GEMTIP model to recover the time constant and surface polarizability coefficients, and prove the good result. The ellipsoidal GEMTIP model is used to recover volume fraction, relaxation parameter and time constant in my study. Figure 4.1 presents the plots of both predicted and measured complex resistivity data using the two-phases ellipsoidal GEMTIP model.

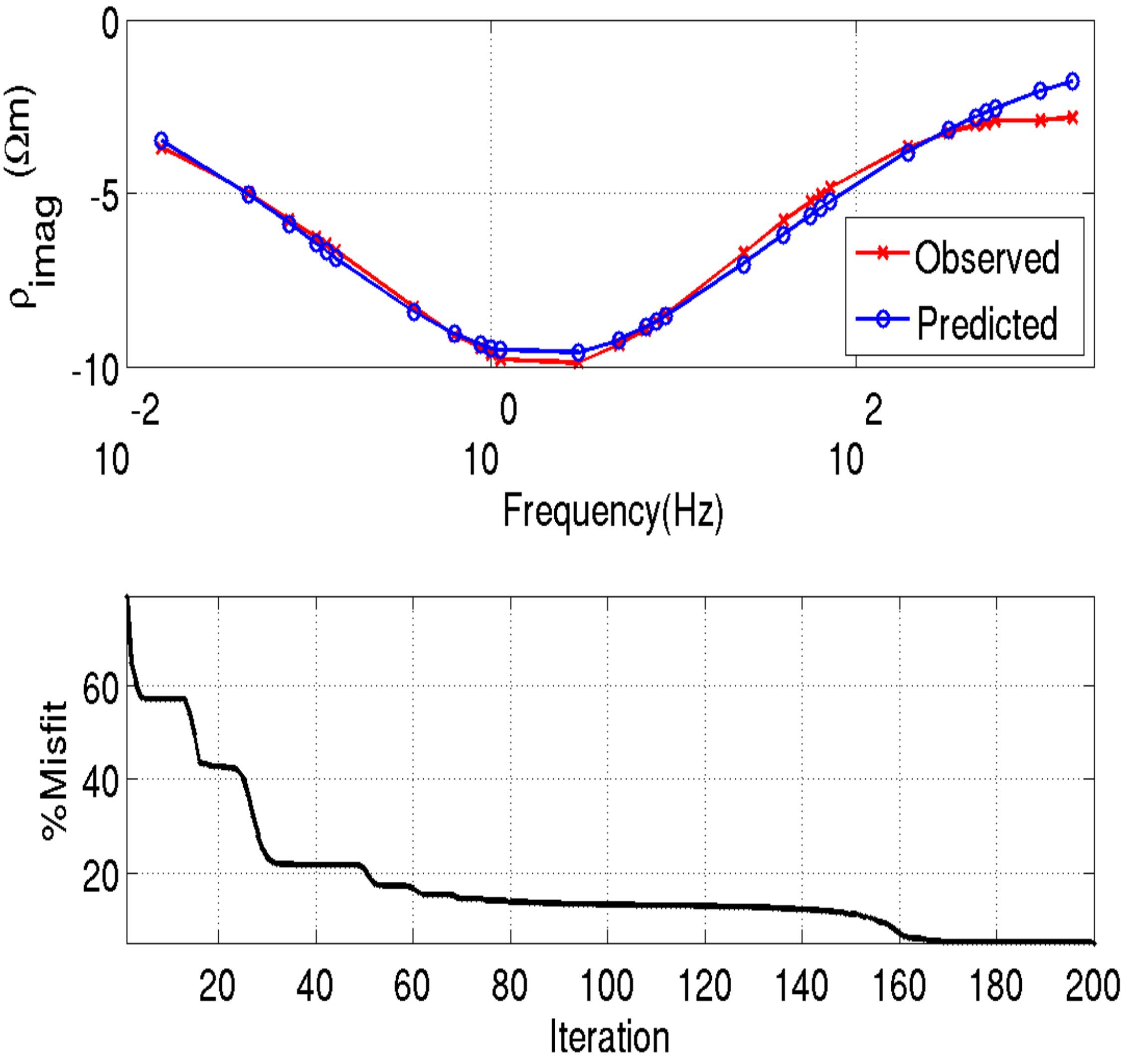

Figure 4.1. Inversion result of sample K01 using the two-phases ellipsoidal GEMTIP model.

Figure 4.2 is a misfit functional of sample K01 plotted with shaded isolines signifying the direction of decreasing misfit. The model steps are plotted using red solid dots. The final model is shown as a solid triangle. Figure 4.3 shows the three-phases model inversion result. The predicted curve fit the observed curve very well, final misfit is 5% and 3.2%, respectively. Table 4.1 shows inversion parameters for sample K01 using the two-phases and three-phases ellipsoidal GEMTIP model. The two-phases recovered volume fraction value is very close to the X-ray measured value. While the three-phases inversion result not only recovered the real volume fraction value, but also separated the different size pyrite, one grain size is 2mm, and another is 1mm.

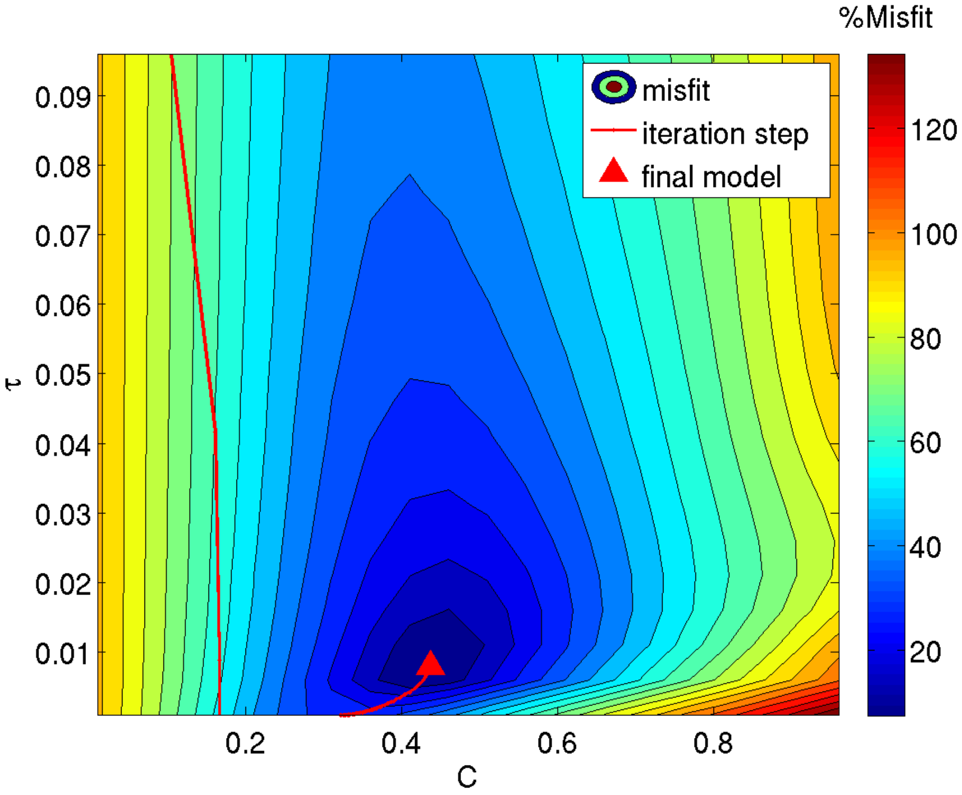

Figure 4.2. The misfit functional of sample K01, plotted with relaxation parameter and time constant.

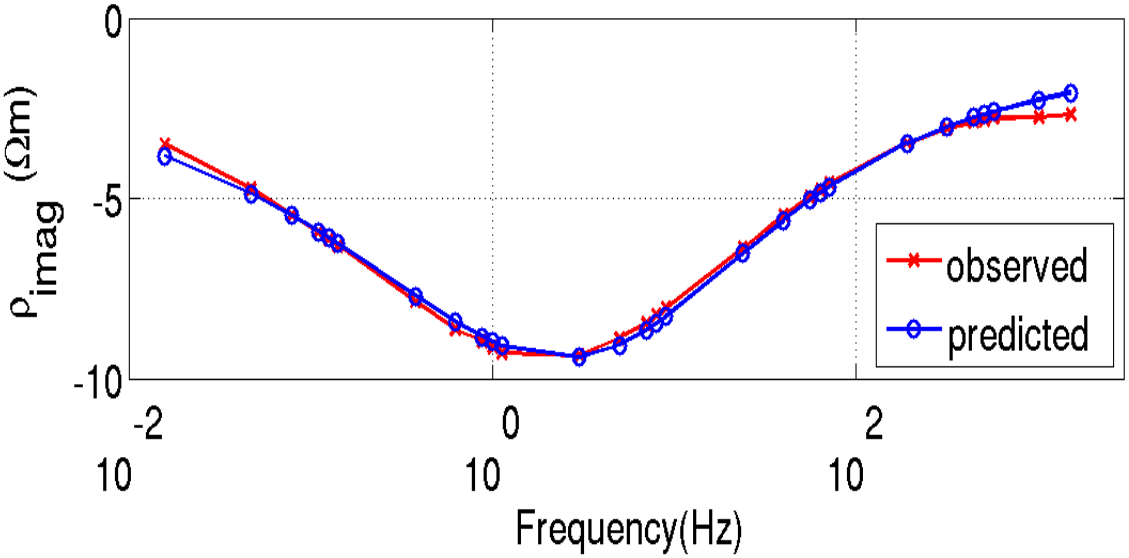

Figure 4.3. Inversion result of sample K01 using the three-phases ellipsoidal GEMTIP model.

Table 4.1 Inversion parameters for sample K01 using the ellipsoidal GEMTIP model

Parameter	Units	Initial value	Two-phases	Three-phases
ρ_{matrix}	Ωm	86	-	87
f_1	%	10	13	3.59
C_1	-	0.1	0.43	0.59
τ_1	seconds	0.1	0.007	0.02
f_2	%	-	-	5.99
C_2	-	-	-	0.21
τ_2	seconds	-	-	0.001

4.1.2 Sample #13

The mineral rock sample #13 is from the Sar Cheshmeh bench 2475 in Iran. This sample contains chalcocite (Cu_2S), chalcopyrite ($CuFeS_2$), and pyrite (FeS_2). Quartz occurs in the veins. Figure 4.4 presents the plot of both predicted and measured resistivity data using the two-phases ellipsoidal GEMTIP model. Figure 4.5 is a misfit functional of sample #13 and shows the parameters relaxation parameter and time constant, plotted with shaded isolines signifying the direction of decreasing misfit.

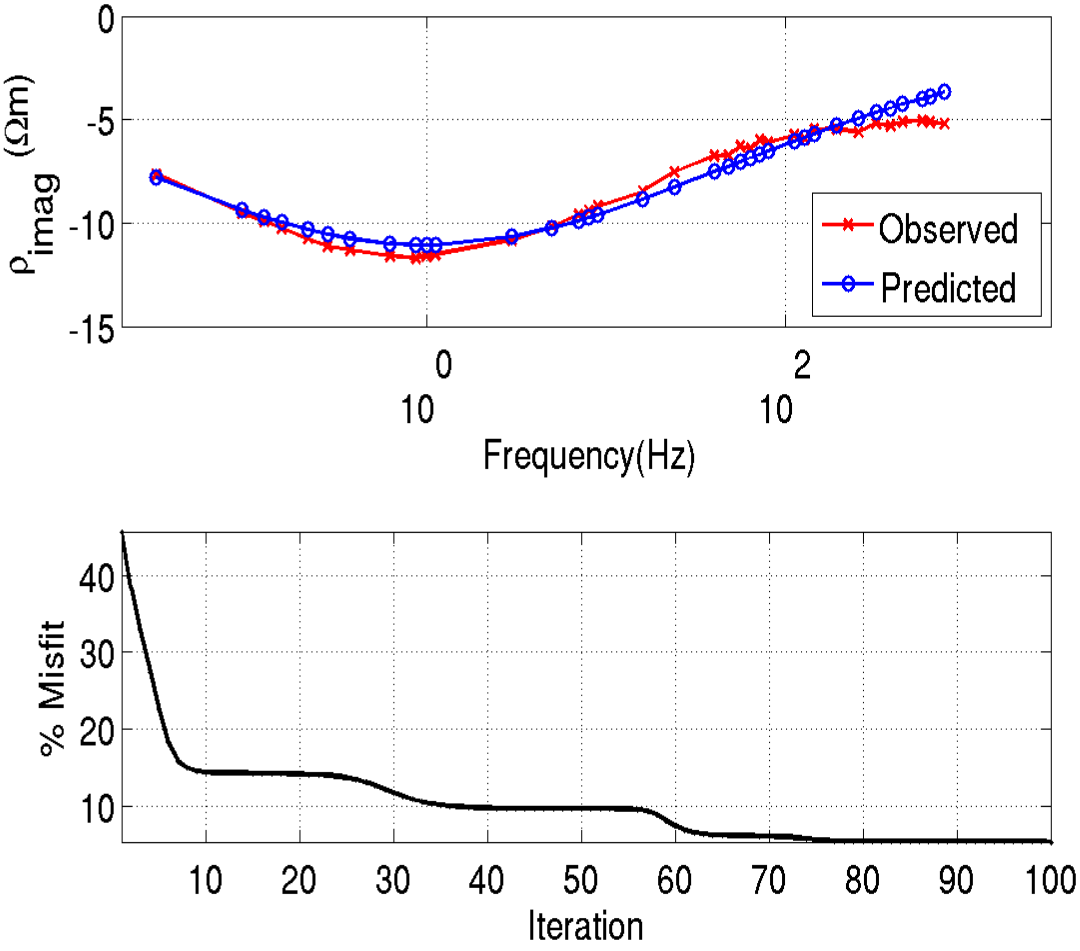

Figure 4.4. Inversion result of sample #13 using the two-phases ellipsoidal GEMTIP model.

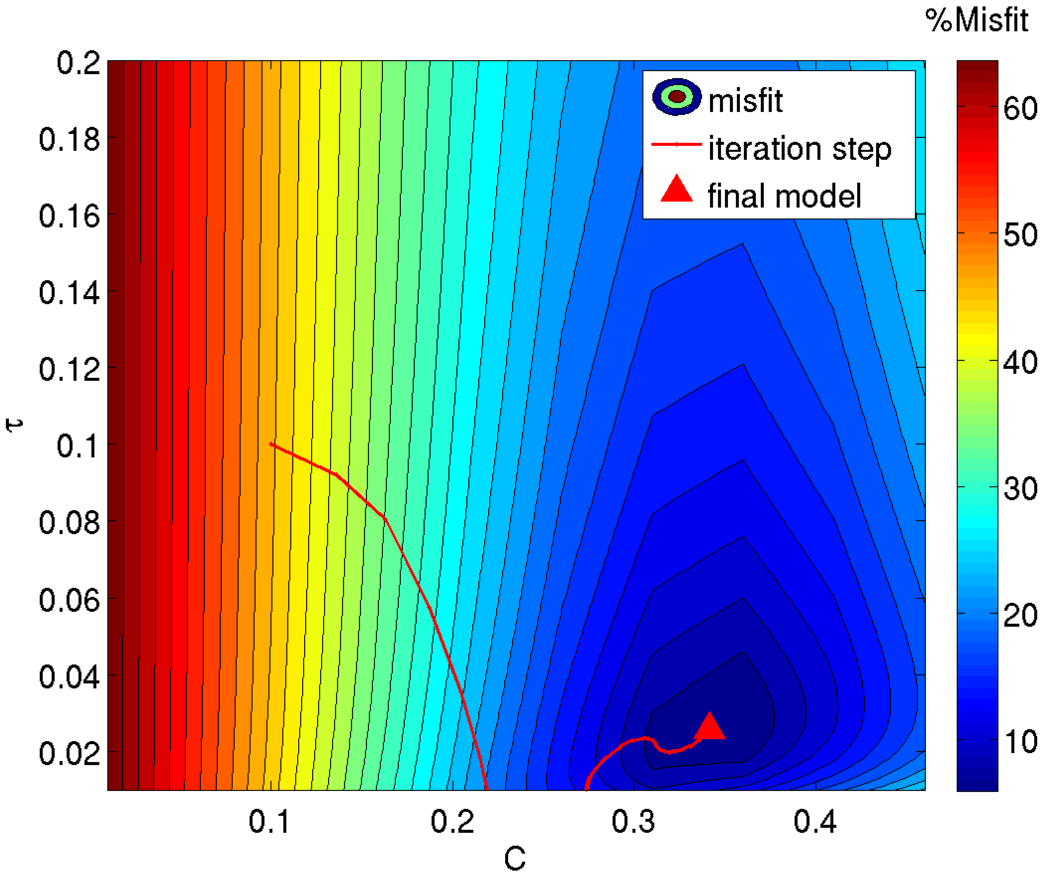

Figure 4.5. The misfit functional of sample #13, plotted with relaxation parameter (C) and time constant (τ).

Figure 4.6 shows the three-phases model inversion result. The parameters of the ellipsoidal GEMTIP model for sample #13 are summarized in Table 4.2. The predicted data fits the measured data with a misfit of 5% and 3.8%, respectively. The two-phases inversion result (6.6%) can recover the total volume fraction, while the three-phases inversion result can separate the pyrite (1.2%) and chalcocite (5%). The recovered volume fraction value is close to the real value from QEMSCAN.

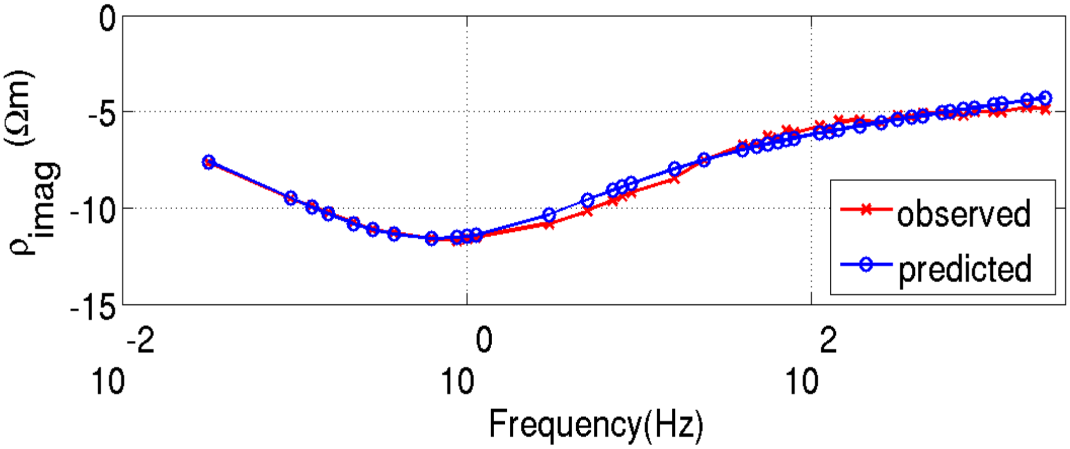

Figure 4.6. Inversion result of sample #13 using the three-phases ellipsoidal GEMTIP model.

Table 4.2 Inversion parameters for sample #13 using the ellipsoidal GEMTIP model

Parameter	Units	Initial value	Two-phases	Three-phases
ρ_{matrix}	Ωm	179	-	188
f_1	%	10	6.6	1.2
C_1	-	0.1	0.34	0.59
τ_1	seconds	0.1	0.025	0.02
f_2	%	-	-	5
C_2	-	-	-	0.21
τ_2	seconds	-	-	0.001

4.2 Shale samples

4.2.1 Sample #8

Sample #8 is a shale-oil sample, the location of depth is 8212.17ft, the effective porosity is 6.63%, gas filled porosity is 6.34%, and the mobile oil saturation is 1.27%. In general, the main IP response recorded of shale rocks will be caused by the membrane polarization, which see the IP effect at a higher frequency (500 to 1000 Hz). About 6.64% of disseminated pyrite is found in this sample by QEMSCAN measurement, it is in sufficient concentrations to produce its own electrode IP peak at lower frequency, and the IP response was observed between 0.01 and 1Hz. But it does not record the membrane polarization at high frequency response. Figure 4.7 shows the observed data along with the predicted data using the two-phases ellipsoidal GEMTIP model.

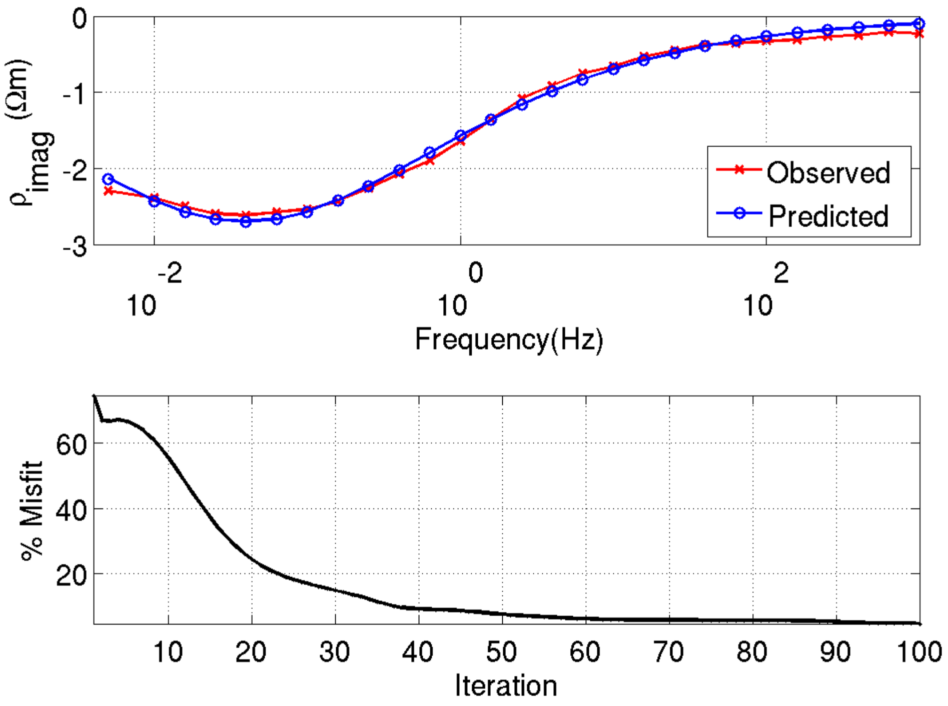

Figure 4.7. Inversion result of sample #8 using the two-phases ellipsoidal GEMTIP model.

Figure 4.8 is a misfit functional of sample #8 plotted with relaxation parameter and time constant. Figure 4.9 shows the inversion result using the three-phases model, but only shows the imaginary part of the data fitting. The final misfit is 5% and 3.2%, respectively. Table 4.3 shows the inversion parameters result. The recovered volume fraction value for the two-phases and three-phases model is close to each other, which is a very reasonable value compared with QEMSCAN pyrite volume fraction (6.64%) and gas filled porosity (6.34%). While the three-phases inversion result exactly separates these two effects, one represents electrode polarization cause by disseminated pyrite, and another phase (4%) represents membrane polarization caused by hydrocarbon.

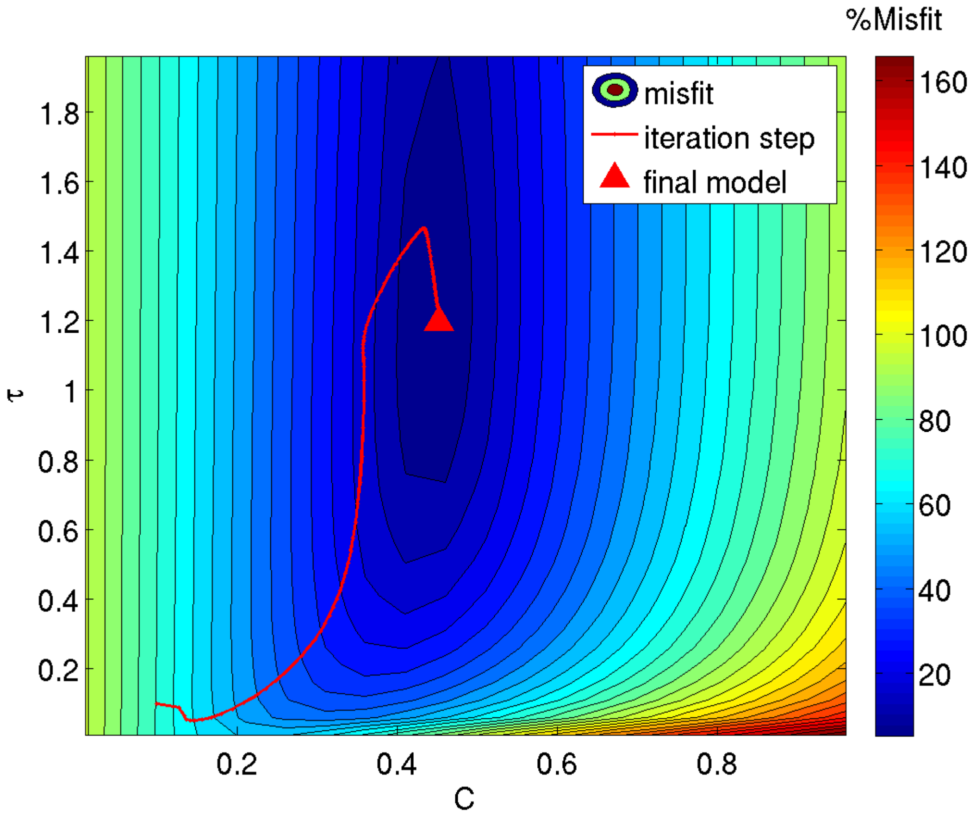

Figure 4.8. The misfit functional of sample #8, plotted with relaxation parameter (C) and time constant (τ).

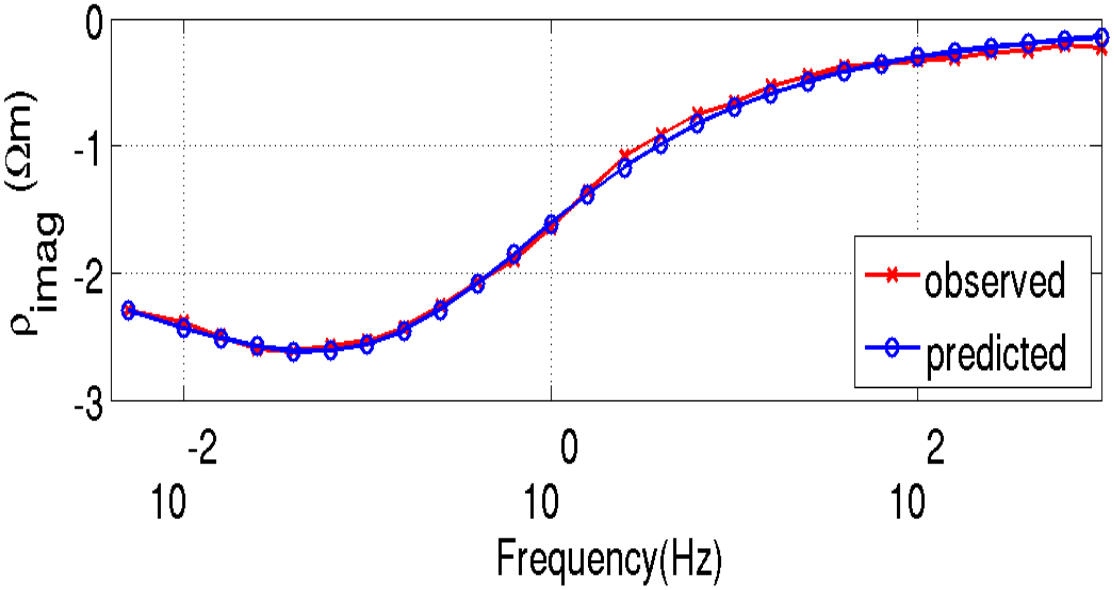

Figure 4.9. Inversion result of sample #8 using the three-phases ellipsoidal GEMTIP model.

Table 4.3 Inversion parameters for sample #8 using the ellipsoidal GEMTIP model

Parameter	Units	Initial value	Two-phases	Three-phases
ρ_{matrix}	Ωm	39	-	30
f_1	%	10	10	6.35
C_1	-	0.1	0.45	0.27
τ_1	seconds	0.1	1.19	2.15
f_2	%	-	-	4
C_2	-	-	-	0.59
τ_2	seconds	-	-	0.46

4.2.2 Sample #33

Sample #33 is a shale-gas sample, the location of depth is 6197.4 ft, the effective porosity is 12.23%, gas filled porosity is 7.98%, the mobile oil saturation is 17.03% and 1.41% of disseminated pyrite was found in this sample by QEMSCAN measurement. The total clay is 0.6%. In this sample, the IP response was observed to be less than 0.01 Hz. However, it does not record the membrane polarization. Figure 4.10 shows the observed data along with the predicted data using the two-phases randomly oriented ellipsoids GEMTIP model.

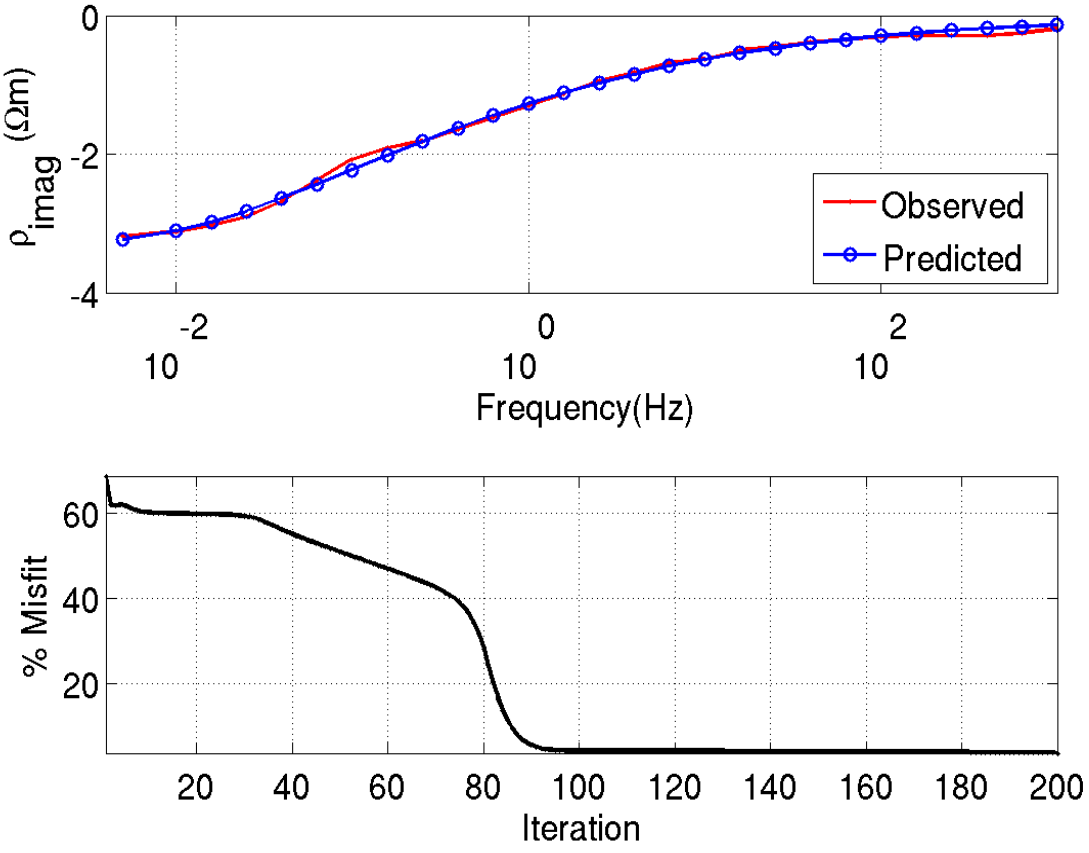

Figure 4.10. Inversion result of sample #33 using the two-phases ellipsoidal GEMTIP model.

Figure 4.11 is a misfit functional of sample #8 plotted with shaded isolines signifying the direction of decreasing misfit. Figure 4.12 shows the inversion result using the three-phases model, but only shows the imaginary part data fitting. Both models predicted data fit the observed data very well. The final misfit is 5% and 3.5%, respectively. Table 4.4 shows the inversion parameters result. The recovered volume fraction value is reasonable in comparison with the known value. The three-phases inversion result separate the pyrite (2.41%) and hydrocarbon (8.11%) very well. The recovered pyrite is a little higher than the real value (1.41%), which is why sample #33 has a calcite matrix, it easily reacts with the solution, and surrounding the pyrite, then increases the pyrite volume fraction.

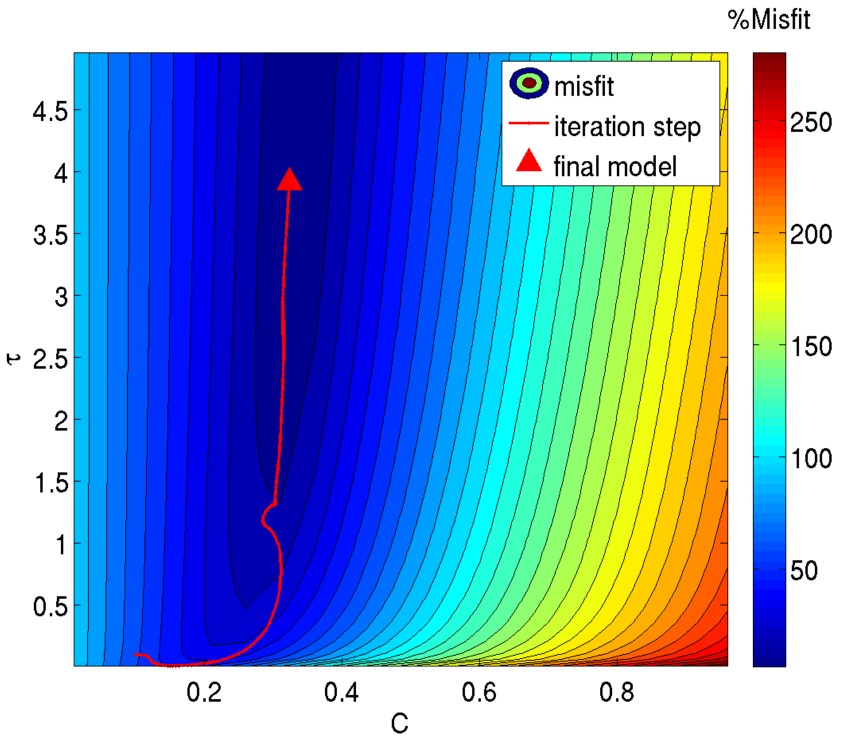

Figure 4.11. The misfit functional of sample #33, plotted with relaxation parameter (C) and time constant (τ).

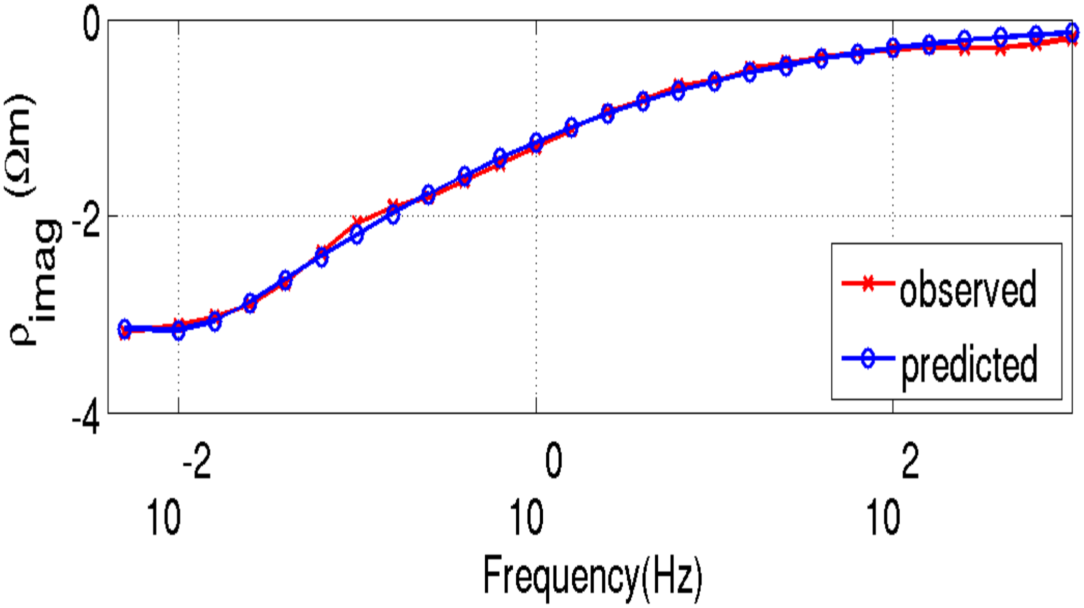

Figure 4.12. Inversion result of sample #33 using the three-phases ellipsoidal GEMTIP model.

Table 4.4 Inversion parameters for sample #33 using the ellipsoidal GEMTIP model

Parameter	Units	Initial value	Two-phases	Three-phases
ρ_{matrix}	Ωm	36	-	46
f_1	%	10	13	2.41
C_1	-	0.1	0.35	0.28
τ_1	seconds	0.1	2.93	8.59
f_2	%	-	-	8.11
C_2	-	-	-	0.43
τ_2	seconds	-	-	3.69

4.2.3 Sample #45

Sample #45 is a laminated shale gas sample, the location of depth is 13843.51 ft, the effective porosity is 2.39%, gas filled porosity is 1.19%, the mobile oil saturation is 33.52%, and 3.53% of disseminated pyrite was found in this sample by the QEMSCAN measurement. In this sample, we can clearly see two IP peaks: one is attributed to its large amount of pyrite grains (electrode polarization), and the IP response was observed at 0.1 Hz, another one is attributed to the hydrocarbon bearing shale (membrane polarization), the IP response was observed at 100 Hz. Figure 4.13 shows the observed data along with the predicted data using the two-phases randomly oriented ellipsoidal GEMTIP model.

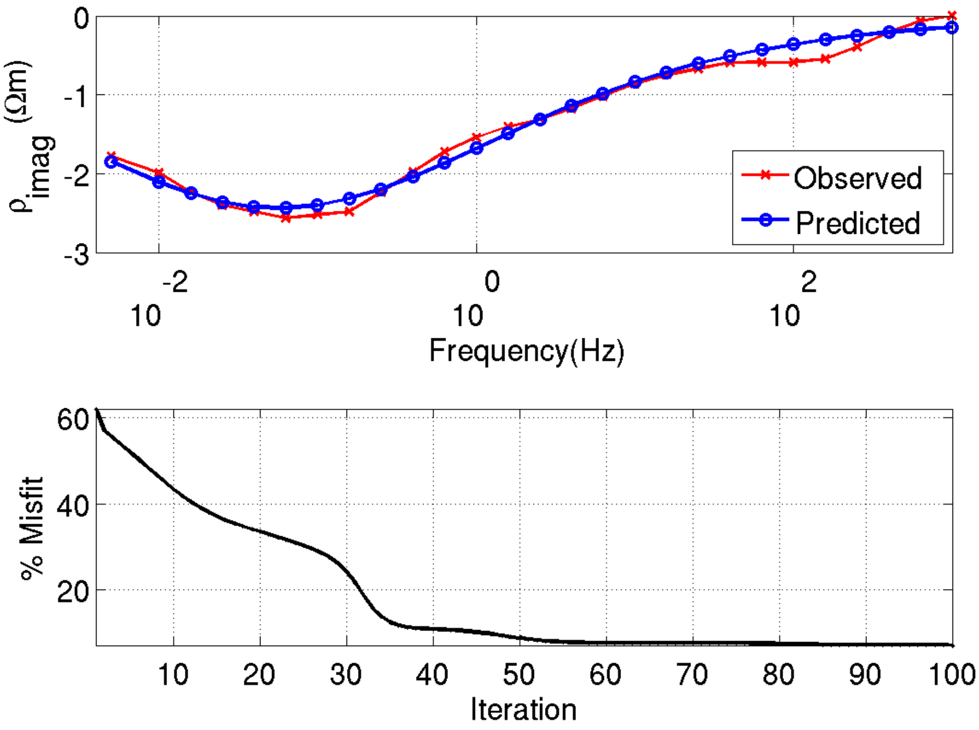

Figure 4.13. Inversion result of sample #45 using the two-phases ellipsoidal GEMTIP model.

Figure 4.14 is a misfit functional of sample #8 plotted with shaded isolines signifying the direction of decreasing misfit. The model steps are plotted using red solid dots. The final model is shown as a solid triangle. Figure 4.15 shows the inversion result using the three-phases model, but only shows the imaginary part data fitting. The predicted data fit the observed data well. Table 4.5 shows the inversion parameters result. The final misfit is 7% and 6.26%, respectively. Both models recovered volume fraction is close to the real value: 3.53% pyrite and 1.19% gas filled porosity. The three-phases inversion result separates the pyrite and hydrocarbon very well.

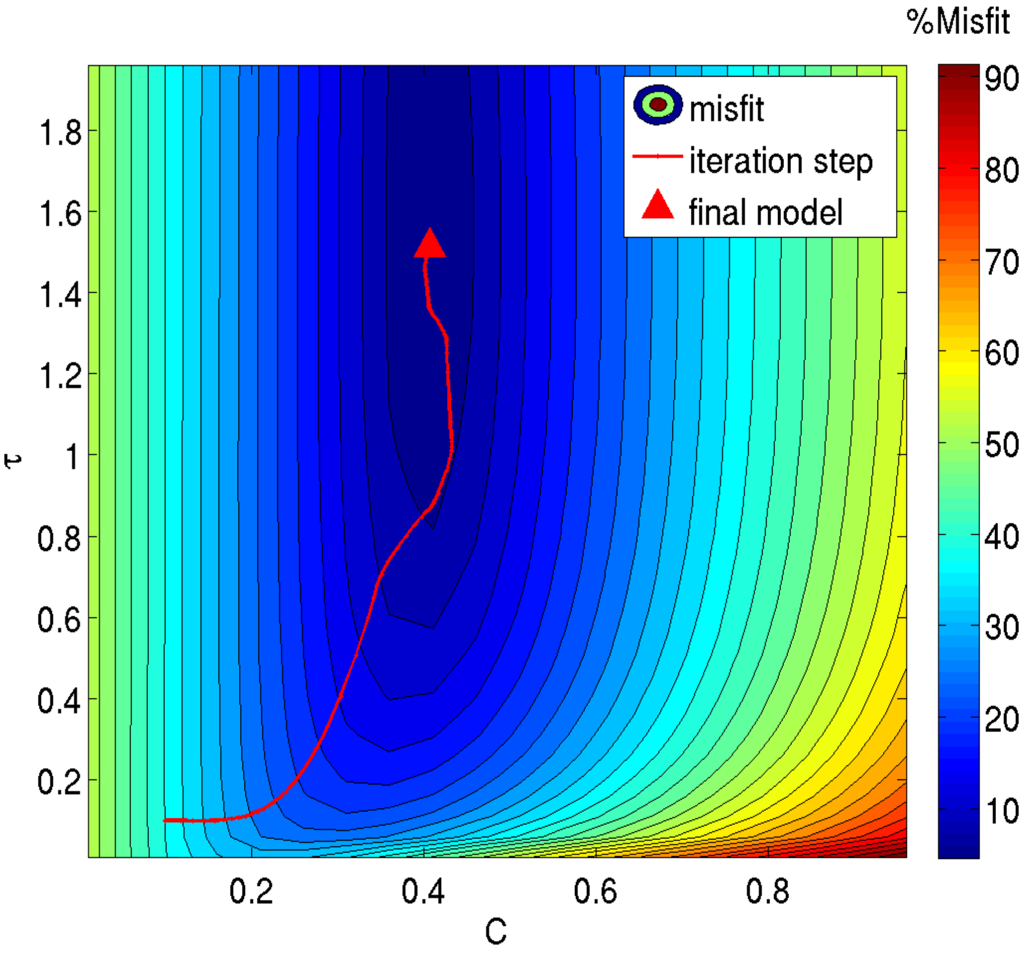

Figure 4.14. The misfit functional of sample #45, plotted with relaxation parameter (C) and time constant (τ).

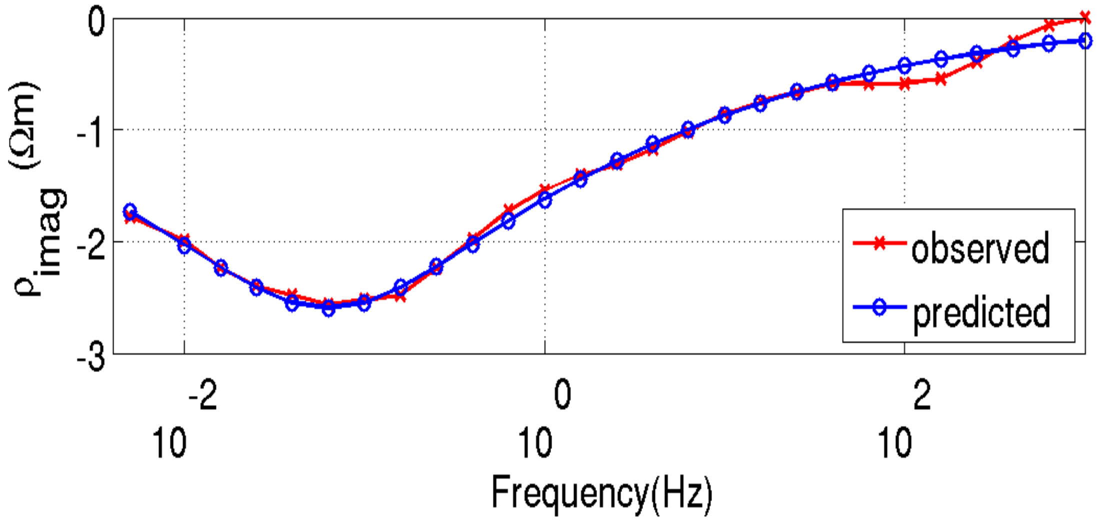

Figure 4.15. Inversion result of sample #45 using the three-phases ellipsoidal GEMTIP model.

Table 4.5 Inversion parameters for sample #45 using the ellipsoidal GEMTIP model

Parameter	Units	Initial value	Two-phases	Three-phases
ρ_{matrix}	Ωm	78	-	89
f_1	%	10	6.6	4.41
C_1	-	0.1	0.42	0.35
τ_1	seconds	0.1	1.55	2.15
f_2	%	-	-	1
C_2	-	-	-	0.77
τ_2	seconds	-	-	1.29

4.3 Discussion

In summary, two igneous rock samples and three shale samples were analyzed using the ellipsoidal GEMTIP model. All tested samples showed IP peaks at relatively low frequencies. Modeling these IP phenomena with two-phases and three-phases ellipsoidal GEMTIP model proved to be very effective, and reasonable inversion results were recovered, especially the volume fraction parameter, which is very close to X-ray microtomography results or QEMSCAN measurement results, however, the three-phases ellipsoidal GEMTIP model can display more.

For two mineral rock samples, the three-phases inversion result of sample K01 not only recovered the real volume fraction value, but also separated the different size minerals. The three-phases inversion result of sample #13 separated the pyrite from chalcocite. For three-shale samples, the three-phases inversion result separated electrode polarization caused by disseminated pyrite and membrane polarization, which was caused by hydrocarbon contained in the shale samples. This study shows that the GEMTIP model can be used in the hydrocarbon bearing shale rocks.

It was also noted by Pelton (1978) that as one decreases the grain size, the time constant also decreases. The inversion result of this study supports this observation. Table 4.6 shows the parameters value of the shale sample. Figure 4.16 shows the plot of relationship time constant and grain size of shale samples. It is found that the time constant increases as the grain size increases.

Table 4.6 GEMTIP parameters value of shale samples

Sample	Pyrite grain size (μm)	Time constant (s)
#8	10.21	1.19
#45	12.39	1.55
#33	13.56	2.93

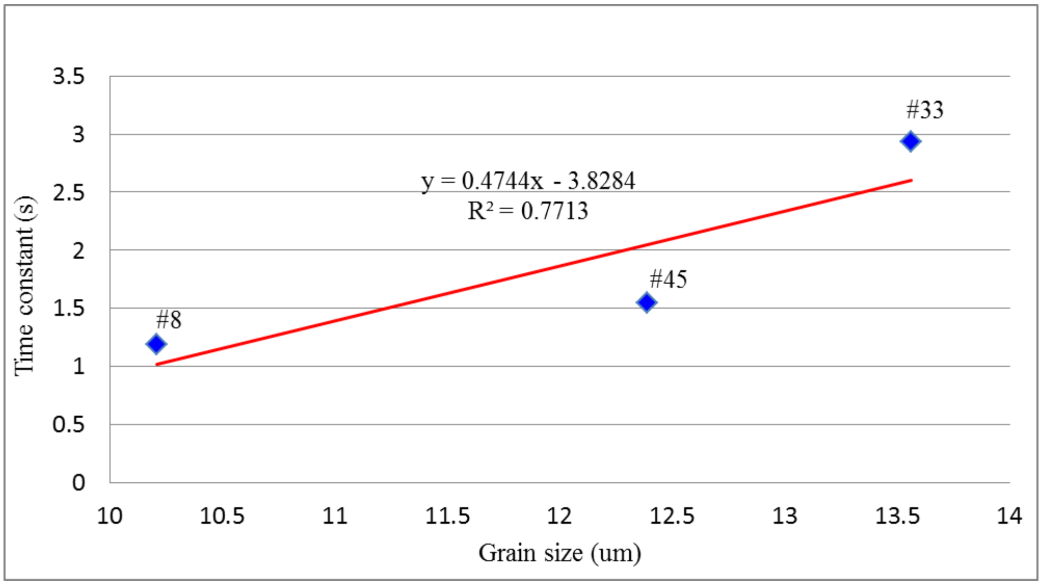

Figure 4.16. Relationship between GEMTIP model parameters of shale samples: time constant vs. grain size.

CHAPTER 5

CONCLUSIONS

A thorough study of complex resistivity of rocks using GEMTIP analysis shows that the exact cause of the IP effect is quite complicated, however, being able to model it can be very useful in improving mineral discrimination techniques. This research focused on the randomly oriented ellipsoidal GEMTIP model. Forward modeling has been done to see how varying individual parameters of the model can affect complex resistivity data. Seeing how the parameters influence the data is very useful for understanding the complex nature of these models.

Two mineral rock and three shale samples containing disseminated sulfides were examined by the ellipsoidal GEMTIP model. Complex resistivity data was obtained by TechnoImaging. Three shale samples and sample #13 were analyzed by QEMSCAN at the University of Utah, Department of Geology and Geophysics. QEMSCAN was used to obtain quantitative values for parameters such as volume fraction, grain type and grain size. All of these measurements combined to form a detailed quantitative analysis of the samples that were then be used for inversion.

The regularized conjugated gradient method was used in a two-phases GEMTIP model inversion, and the extensive search method was used in a three-phases GEMTIP model inversion, reasonable inversion results were recovered. The geologic information from QEMSCAN provides a good comparison with recovered parameters (volume fraction). By comparing the two-phases with the three-phases inversion results, the mineral rock samples study shows that the three-phases GEMTIP model can separate the different mineral sizes and different mineral types from the same sample; the shale samples show the three-phases GEMTIP model can separate the membrane polarization, caused by the internal structure of the shale samples, from electrode polarization caused by disseminated pyrite. This study shows that the GEMTIP model can be used in hydrocarbon bearing shale rocks. The inversion recovered parameters time constant shows that as the grain size increases the time constant also increases.

In the future, it would be useful to continue collecting complex resistivity data sets for shale samples in order to further analyze the relationship between GEMTIP model parameters and actual rock characteristics. For example, relationships between grain size and volume fraction, relationships between grain size and relaxation parameters are very important factors in identifying minerals for geophysicist. Lots of sample studies can find a direct correlation between GEMTIP model parameters and mineral type. The application of GEMTIP model will be a good tool for mineral exploration.

APPENDIX A

INVERSION RESULT

The following tables contain two-phases and three-phases GEMTIP model parameters value and inversion results of all samples used in the project. ρ_0 is matrix resistivity, a_l is the grain size of l_{th} type mineral, e_l is ellipticity of the l_{th} type mineral, f_l is volume fraction of the l_{th} type mineral, C_l is the relaxation parameter of the l_{th} type mineral, τ_l is time constant of the l_{th} type mineral, β_l is surface polarizability coefficient of the l_{th} type mineral. Two-phases model $l = 1$, Three-phases model $l = 1, 2$.

Table A.1 Two-phases inversion result

Parameter	Units	K01	#13	#8	#33	#45
ρ_0	Ωm	86	179	39	36	78
a_1	mm	1	0.05	0.001	0.001	0.01
e_1	-	10	10	6.4	10	10
f_1	%	13	6.6	10	13	6.6
C_1	-	0.43	0.34	0.45	0.35	0.42
τ_1	s	0.007	0.025	1.19	2.93	1.55
β_1	$\Omega m.\, m/_{s^{c_l}}$	0.3	0.015	0.00022	0.00013	0.00034

Table A.2 Three-phases inversion result

Parameter	Units	K01	#13	#8	#33	#45
ρ_0	Ωm	80	188	30	46	89
a_1	mm	1	0.05	0.01	0.013	0.01
e_1	-	10	10	10	10	2.3
f_1	%	3.59	1.2	6.35	2.4	4.4
C_1	-	0.59	0.59	0.28	0.28	0.77
τ_1	s	0.022	0.16	2.15	3.69	2.15
β_1	$\Omega m.\, m/s^{c_1}$	0.5	0.013	0.00012	0.0002	0.0002
a_2	mm	2	0.1	0.001	0.001	0.001
e_2	-	10	10	10	3.9	1
f_2	%	5.99	5	4	8.1	1
C_2	-	0.22	0.22	0.59	0.43	0.35
τ_2	s	0.001	0.001	0.46	8.5	1.29
β_2	$\Omega m.\, m/s^{c_1}$	0.5	0.013	0.00012	0.0002	0.0002

APPENDIX B

LIST OF ELECTRONIC DATA

The included DVD-Data disk contains EM Data, QEMSCAN data, MATLAB codes, figures, and thesis source files.

Folder: CODE

Contains MATLAB codes used to create every plot of forward modeling, synthetic data study and inversion.

Folder: DATA

Contains CR measurements for all rock samples in the form of .xlsx files and QEMSCAN result in the form of .pptx file.

Folder: FIGURE

Contains the pictures used in this thesis in the form of .tif and .vsd files.

Folder: THESIS

Contains the thesis paper in the form of .pdf and .pptx file.

REFERENCES

Ayling, B., Rose, P., Petty, S., Zemach, E., and Drakos, P., 2012, QEMSCAN: Capability and application to fracture characterization in geothermal systems: Proceeding, Thirty-Seventh Workshop on Geothermal Reservoir Engineering, SGP-TR-194.

Buist, S., 2009, Induced polarization effect in land and marine CSEM data: Applications for hydrocarbon exploration [M.S. thesis]: Salt Lake City, University of Utah.

Burtman, V., Gribenko, A., and Zhdanov, M.S., 2010, Advances in experimental research of induced polarization effect in reservoir rocks: 80th Annual International Meeting, SEG, Expanded Abstracts, p. 2475–2479.

Burtman, V., Zhdanov, M.S., Gribenko, A., and Dmitriev, V.I., 2008, Anisotropy of induced polarization in the context of the generalized effective-medium theory: 78th Annual International Meeting, SEG, Expanded Abstracts, p. 677–681.

Burtman, V., Endo, M., Zhdanov, M.S., and Ingeman-Nielsen, T., 2011, High-frequency induced polarization measurements of hydrocarbon-bearing rocks: 81st Annual International Meeting, SEG, Expanded Abstracts, p. 677–681.

Cole, K.S., and Cole, R.H. 1941, Dispersion and absorption in dielectrics: Journal of Chemical Physics, v. 9, p. 343-351.

Emond, A., 2007, Electromagnetic modeling of porphyry systems from the grain-scale to the deposit-scale using the generalized effective medium theory of induced polarization [M.S. thesis]: Salt Lake City, University of Utah.

Emond, A., Zhdanov, M.S., and Petersen, E.U., 2006, Electromagnetic modeling based on the rock physics description of the true complexity of rocks: Applications to porphyry copper deposits: 76th Annual International Meeting, SEG, Expanded Abstracts, p. 1313-1317a.

Fu, L., 2011, Induced polarization effect in time domain: Theory, modeling and applications [M.S. thesis]: Salt Lake City, University of Utah.

Gottlieb, P., Wilkie, G., Sutherland, D., Ho-Tun, E., Suthers, S., Perera, K., Jenkins, B., Spencer, S., Butcher, A., and Rayner, J., 2000, Using quantitative electron microscopy for process mineralogy applications. Journal of the Minerals, Metals and Materials Society, v. 52(4), p. 24-25.

Kearey P., Brooks, M., and Hill, I., 2002, An Introduction to Geophysical Exploration: Blackwell Science.

Kiberu J., 2002, Induced polarization and resistivity measurements on a suite of near surface soil samples and their empirical relationship to selected measured engineering parameters [M.S. thesis]: Enschede, International Institute for Geo-information Science and Earth Observation.

Luo, Y., and Zhang, G., 1998, Theory and application of spectral induced polarization: SEG.

Madden, T.R., and Marshall, D.J., 1958, A laboratory investigation of induced polarization: A.E.C. report RME-3156.

Pelton, W.H., Ward, S.H., Hallof, P.G., Sills, W.R., and Nelson, P.H., 1978, Mineral discrimination and removal of inductive coupling with multi-frequency IP: Geophysics, v. 43, p. 588-609.

Reynolds, J.M., 1997, An Introduction to Applied and Environmental Geophysics: Wiley.

Sliwinski, J., Power, M., Hughes P., and Harrington, J., 2010, Integrated Shale Gas Evaluation: A study of QEMSCAN, SEM and Optical Petrography, XRD and Geochemistry of selected potential and producing North American Gas Shales: GeoCanada 2010.

Sumner, J.S., 1976, Principles of Induced Polarization for Geophysical Exploration: Elsevier.

Zhdanov, M.S., 2002, Geophysical Inverse Theory and Regularization Problems: Elsevier.

Zhdanov, M.S., 2005, New geophysical technique for mineral exploration and mineral discrimination based on electromagnetic methods, U. S. Patent application, U-3885.

Zhdanov, M.S., 2008, Generalized effective-medium theory of induced polarization: Geophysics, v. 73, p. 197-211.

Zhdanov, M.S., 2009, Geophysical electromagnetic theory and methods: Elsevier.

Zhdanov, M.S., and Burtman, V., 2009, Induced polarization in hydrocarbon-saturated sands and sandstones: Experimental study and general effective medium modeling: 79th Annual International Meeting, SEG, Expanded Abstracts, p. 774–778.

Zhdanov M.S., Burtman, V., Gribenko, A., and Phillips, R., 2009, Analysis of isotropic and anisotropic IP response of rocks based on the generalized effective-medium theory: Proceedings of the Annual Meeting of the Consortium for Electromagnetic Modeling and Inversion, University of Utah, p. 71-96.

Zhdanov M.S., Burtman, V., Endo, M., and Wilson, G.A., 2012, Laboratory-based GEMTIP analysis of spectral IP data for mineral discrimination: 82ed Annual International Meeting, SEG.